Title

Mechanistic Insights into Co and Fe Quaterpyridine-Based CO2 Reduction Catalysts: Metal–Ligand Orbital Interaction as the Key Driving Force for Distinct Pathways

Journal

Journal of the American Chemical Society, 143(2)

ISSN

0002-7863

Authors

Loipersberger, Matthias
Cabral, Delmar GA
Chu, Daniel BK
et al.

Publication Date

2021-01-20

DOI

10.1021/jacs.0c09380

Peer reviewed

Mechanistic Insights into Co and Fe Quaterpyridine Based CO_2 Reduction Catalysts: Metal-Ligand Orbital Interaction as the Key Driving Force for Distinct Pathways

Matthias Loipersberger,*,† Delmar G. A. Cabral ,† Daniel B. K. Chu,‡,¶ and Martin Head-Gordon*,†,§

†*Department of Chemistry, University of California, Berkeley, California 94720, USA*

‡*Department of Chemical Engineering, University of California, Santa Barbara, California 93106, USA*

¶*Present address: Department of Chemical Engineering, Massachusetts Institute of Technology, Cambridge, Massachusetts 02139, USA*

§*Chemical Sciences Division, Lawrence Berkeley National Laboratory, Berkeley, California 94720, USA*

E-mail: m.loipersberger@berkeley.edu; mhg@cchem.berkeley.edu

Abstract

Both $[Co^{II}(qpy)(H_2O)_2]^{2+}$ and $[Fe^{II}(qpy)(H_2O)_2]^{2+}$ (with qpy = 2,2′:6′,2″:6″,2‴-quaterpyridine) are efficient homogeneous electrocatalysts and photoelectrocatalysts for the reduction of CO_2 to CO. The Co catalyst is more efficient in the electrochemical reduction while the Fe catalyst is an excellent photoelectrocatalyst (*ACS Catal.* **2018**,*8*, 3411–3417). This work uses density functional theory to shed light on the contrasting catalytic pathways.

While both catalysts experience primarily ligand-based reductions, the second reduction in the Co catalyst is delocalized onto the metal via a metal-ligand bonding interaction, causing a spin transition and distorted ligand framework. This orbital interaction explains the experimentally observed mild reduction potential and slow kinetics of the second reduction. The decreased hardness and doubly occupied d_{z^2}-orbital facilitate a σ-bond with the CO_2-π^* in an η^1-κC binding mode. CO_2 binding is only possible after two reductions resulting in an EEC mechanism (E=electron transfer, C=chemical reaction), and the second protonation is rate-limiting.

In contrast, the Fe catalyst maintains a Lewis acidic metal center throughout the reduction process because the metal orbitals do not strongly mix with the qpy-π^* orbitals. This allows to bind the activated CO_2 in an η^2 binding mode. This interaction stabilizes the activated CO_2 via a π-type interaction of a Fe-t_{2g} orbital and the CO_2-π^* and a dative bond of the oxygen lone pair. This facilitates CO_2 binding to a singly reduced catalyst resulting in an ECE mechanism. The barrier for CO_2 addition and the second protonation are higher than those for the Co catalyst and rate-limiting.

Introduction

The electrochemical reduction of CO_2 to CO is a promising pathway for sustainable fuel production via artificial photosynthesis.[1–3] The resulting carbon monoxide can be further transformed into hydrocarbons using the Fischer-Tropsch process,[4] making it one of the most economically viable products of CO_2 reduction out of a variety of possible products.[5] Carbon dioxide is typically electrochemically inert, so proton coupled reductions are necessary to operate at moderate potentials. Unfortunately, the two-electron two-proton CO_2 reduction reaction (CO2RR) to CO operates at a potential similar to the less desirable hydrogen evolution reaction (HER).[6,7] Consequently, catalysts are required which are ideally efficient (low overpotential), fast (high turnover frequency (TOF)), substrate selective (CO2RR vs HER), and cheap (earth abundant materials).

The main catalytic[6] approaches are molecular,[8–12] heterogeneous[13,14] and biological.[15] Heterogeneous catalysts reduce CO_2 with high current densities,[16] but often suffer from poisoning and poor substrate selectivity.[6,13,14,17] For example, copper is able to reduce CO_2 with a high current density but produces a variety of C1 and C2 products with ethylene and ethanol as the main products,[13,18] making mechanistic studies difficult.[19,20]

Homogeneous catalysts can facilitate electron transfer to CO_2 yielding lower overpotentials. Furthermore, the catalyst can stabilize various intermediates and transition states to accelerate the transformation of CO_2. Molecular catalysts yield good TOF, a very high selectivity (over 90%), and are highly tunable.[21–23] The activity of the molecular catalyst can be dramatically improved by a novel flow cell design. Berlinguette *et al.* designed a zero-gap membrane flow reactor which produced CO (from CO_2) using a cobalt phthalocyanine catalyst, achieving a current density comparable to a heterogeneous catalyst and a selectivity of over 95%.[24] Alternatively, activity can be improved by incorporating the catalyst into metal/covalent organic frameworks[25–28] or attaching the molecular catalyst onto a surface.[29–34]

Mechanistic insights in the catalytic pathway are invaluable for rational catalyst design as they illuminate the origin of activity and selectivity, as well as the cause of any intrinsic limitations. Both spectroscopic methods and computational chemistry should be employed to identify possible intermediates, steps in the reaction pathway, activation barriers, and rate limiting steps. Experimental tools include cyclic voltammetry (CV),[35,36] Mössbauer, EPR,[37] X-ray spectroscopy/ crystallography,[38,39] spectroelectrochemistry,[40] and stopped-flow rapid mixing and transient absorption[41] (see references [42] & [10] for a detailed overview). Computational methods such as density functional theory[43–46] (DFT) can provide structural and spectroscopic information on intermediates along with complete catalytic pathways by computing reaction free energies, reduction potentials, pK_a values, and barrier heights among many examples. Detailed computational studies providing mechanistic insights were conducted, for example, by Ye *et al.* for the nickel cyclam system[47] and Carter *et al.* for the

rhenium/manganese tricarbonyl-bipyridine system.[48–50]

The most prominent molecular catalysts for the electrochemical reduction of CO_2 to CO are nickel cyclam,[51–54] rhenium/manganese tricarbonyl-bipyridine [55–64] and iron porphyrins such as FeTPP (TPP = tetraphenylporphyrin) and its derivatives .[65–69] Both iron and cobalt catalysts are especially desirable due to the natural abundance of the central metal, and notable iron[70,71] and cobalt[72] based catalysts were developed recently. This makes iron[73] and cobalt[74] quaterpyridine complexes especially attractive as both complexes are active CO_2 reduction catalysts with an identical ligand framework. Both catalysts are efficient and selective, meaning both catalysts (or their derivatives) find application in electrochemical[75–77] and photoelectrochemical[78] reduction of CO_2 to various products, even to CH_4 (albeit with a low Faradaic efficiency);[79] furthermore, hybrid systems are able to operate efficiently in water.[30,80]

Robert *et al.*[75] reported a detailed experimental mechanistic study to investigate the catalytic pathways of both Fe and Co systems. Interestingly, they proposed distinct pathways despite an identical ligand framework (see figures 1 (a) and (b)). Therefore, this system provides a unique opportunity to understand the role of the central metal for each step throughout a catalytic pathway. In this work, we provide a computational study where we propose detailed catalytic pathways for both metals in line with the experimental findings of reference [75] (compare figures 1 (a) and (b) with figures 3 and 9). Furthermore, we provide an in-depth analysis of the electronic structure of important intermediates to understand the origin of the different pathways and reactivities, and predict the effect of ligand substituent groups on the key steps.

Experimental Findings

Robert *et al.*[75] reported two selective and efficient catalysts for the electrochemical reduction of CO_2 to CO: $[Co^{II}(qpy)(H_2O)_2]^{2+}$ and $[Fe^{II}(qpy)(H_2O)_2]^{2+}$ with qpy = 2,2′:6′,2″:6″,2‴-quaterpyridine. The cobalt catalyst shows fast turnover rates (500–33000 s^{-1}). Both are

extremely selective for CO2RR over HER (>95%) and operate at low overpotentials (140–240 mV). Furthermore, both are also highly selective and active catalysts for the photochemical conversion of CO_2 to CO with selectivity and turnover numbers up to 2600.[78] Interestingly, experimental evidence suggests that the two catalysts exhibit different pathways despite the identical ligand framework. The experimentally suggested pathway for $[Co^{II}(qpy)(H_2O)_2]^{2+}$ is as follows: (i) two reductions to form a $[Co(qpy)]^0$ intermediate; (ii) binding of CO_2 resulting in a $[Co(qpy)CO_2]^0$ intermediate; (iii) two protonation steps involving the C−O bond cleavage and CO release to close the cycle (see figure 1 (a)). The suggested pathway for $[Fe^{II}(qpy)(H_2O)_2]^{2+}$ differs: (i) initial reduction resulting in an $[Fe(qpy)]^+$ intermediate; (ii) binding of CO_2 to form a $[Fe(qpy)CO_2]^+$ intermediate; (iii) two protonation and reduction events cleaving one C−O bond of CO_2 to form H_2O and a singly reduced $[Fe(qpy)CO]^+$ adduct; (iv) release of CO to close the cycle (see figure 1 (b)). The experimental evidence is summarized in the following paragraphs (potentials were reported versus SCE but are converted in this work against ferrocene/ferrocenium couple (Fc^+/Fc) for consistency using −380 mV[81]).

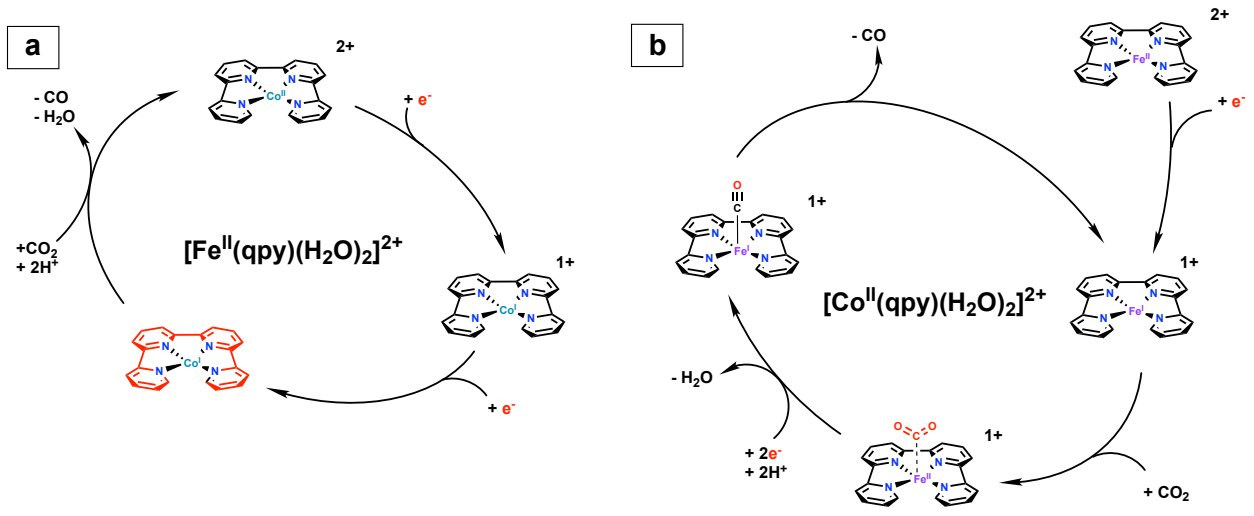

Figure 1: Proposed catalytic pathways by Robert *et al.*[75] for both (a) $[Fe^{II}(qpy)(H_2O)_2]^{2+}$ and (b) $[Co^{II}(qpy)(H_2O)_2]^{2+}$ based on experimental observations; the red colored molecular moiety indicates localization of the excess electrons.

The cobalt based catalyst $[Co^{II}(qpy)(H_2O)_2]^{2+}$ exhibits two reduction waves at −0.95 V

and −1.18 V vs Fc^+/Fc. The first reduction wave is reversible, but the second wave is only observable at low scan rates, suggesting that a slow water loss occurs before the second reduction. The addition of phenol during the CV experiments results in coordination of the acid to the metal center which shifts the second reduction wave to −1.66 V vs Fc^+/Fc. The presence of CO_2 does not induce a shift of the first reduction wave. This indicates no binding of CO_2 after only one reduction which is in contrast to the iron system. Controlled potential electrolysis (CPE) at −1.5 V in wet acetonitrile (2% water) with electrolyte ions and 3 M PhOH showed high selectivity (96% CO and 4% H_2) and a high Faradaic efficiency (FE) of 94%. $[Co^{II}(qpy)(H_2O)_2]^{2+}$ ranks among the fastest homogeneous CO_2 reduction catalysts reported to date with a TOF_{max} up to 33000 s^{-1} and an overpotential of 300 mV. This can be compared to the fastest molecular catalyst for CO_2 to CO reduction: Fe-*o*-TMA, a tetra-TMA substituted FeTPP derivative (TMA = trimethylammonio, $-NMe_3^+$), with a TOF_{max} of up to 10^6 s^{-1} at an overpotential of 220 mV.[69] A second top performing system is $[Mn(mesbpy)(CO)_3(MCN)]^+$ (mesbpy = dimesityl-2,2′-bipyridine) with a TOF_{max} 630 s^{-1} at an overpotential of 300 mV.[82] It is important to point out that both the FeTPP[39,65–69,83–86] and Mn/Re$(bpy)(CO)_3$[48–50,55–64,82] systems were extensively studied and thus have optimized ligand frameworks and reaction conditions unlike the $[Co^{II}(qpy)(H_2O)_2]^{2+}$ and $[Fe^{II}(qpy)(H_2O)_2]^{2+}$ systems; see references[69],[75] and[82] for benchmarking Tafel plots including more (less active) catalysts. A second study[76] on $[Co^{II}(qpy)(H_2O)_2]^{2+}$ revealed that an alternative pathway for CO2RR under different conditions is feasible: at lower acid concentrations (0.1 M PhOH) and a higher applied potential (−1.98 V vs Fc^+/Fc), a second pathway via a triply reduced catalyst is accessible. However, both FE (77%) and selectivity against HER (77% CO and 20% H_2) are decreased.

$[Fe^{II}(qpy)(H_2O)_2]^{2+}$ exhibits a reversible first reduction wave at −1.39 V vs Fc^+/Fc and a second reversible reduction at −1.60 V vs Fc^+/Fc under argon atmosphere. The first reduction wave is positively shifted by 0.021 V and becomes irreversible upon saturation with CO_2. This suggests an EC mechanism: electron transfer (E) followed by the chemical (C)

addition of CO_2 to the iron catalyst. The rate constant was estimated as 82 $s^{-1}M^{-1}$ based on the scan rate dependence of the shift (assuming pure kinetic conditions). This corresponds to an activation energy of ∼15 kcal/mol (using transition state theory). Catalysis is observed after the second reduction at approximately −1.60 V vs Fc^+/Fc and is enhanced with an acid (phenol). On the backward scan an oxidation wave at −1.09 V vs Fc^+/Fc was observed. The shift to more anodic potentials is attributed to a singly reduced carbonyl species $[Fe(qpy)CO]^+$. The presence of this carbonyl species is further established by CV experiments under CO atmosphere where a reversible reduction wave at −1.17 V vs Fc^+/Fc is observed, suggesting an EC sequence. In addition, a second reduction wave is observed at −1.42 V vs Fc^+/Fc which corresponds to the reduction of the singly reduced $[Fe(qpy)CO]^+$ species. CPE at −1.6 V vs Fc^+/Fc (240 mV overpotential) in wet acetonitrile (2% water) and 1 M PhOH showed that the catalyst produces CO with over 99% selectivity but with a low Faradaic efficiency of 48%. However, the FE can be improved to 70% by irradiation with visible light during the electrolysis. It is conjectured that light promotes CO release from the $[Fe(qpy)CO]^+$ intermediate over further reduction to $[Fe(qpy)CO]^0$.

Computational Model

All quantum chemical calculations were performed with the Q-Chem package[87] (version 5.2.0) using the ωB97X-D[88] density functional for all Fe compounds and the B3LYP-D3[89–92] density functional for all Co compounds. All DFT calculations use a (75, 302) grid (75 radial shells with 302 Lebedev points on each) for the integration of the exchange-correlation functional. The reason for choosing different functionals is to ensure that the predicted reduction potentials are in good agreement with the experimentally reported values (see below for further discussion). Minima and transition state (TS) geometries were verified as stationary points by harmonic vibrational frequencies.

The geometry optimization and frequency calculations employed a mixed basis (def2-

SVP for N,C,H, def2-SVPD for O and def2-TZVP basis set for Fe and Co).[93] Single point calculations were performed with the larger def2-TZVPPD basis[93] to decrease the basis set incompleteness errors, consistent with best practices.[45]

The solvation energies were calculated using the C-PCM model (acetonitrile, $\epsilon = 35.88$) as implemented in Q-Chem.[94] All molecular orbitals (MOs) were plotted using an isovalue of 0.03 (blue: positive, red: negative values) and spin densities were visualized using an isovalue of 0.005 (green: α spin density, gold: β spin density).

The reaction free energies ($\Delta_R G$), activation energies ($\Delta G^{\ddagger}$), reduction potentials, and pK_a values were calculated based on the standard thermodynamic cycles.[47] The Gibbs free energies include enthalpic contributions from the zero-point energy correction and the entropic contribution, which is calculated from the vibrational frequencies at T = 298 K. Solvation energies were approximated using single point calculations with the implicit C-PCM solvent model.

The gas phase rigid rotor and harmonic oscillator approximations were used for the entropic contribution to the free energies of CO_2 binding. It is known that this approach can overestimate entropies for species in solution because both translational and rotational degrees of freedom are reduced by surrounding solvent molecules. The comparison with experimental entropies (obtained via Henry's Law) indicate differences of up to 9 kcal/mol for the free energy of CO_2 in solution.[95,96] This implies that calculated CO_2 binding free energies are too endergonic.

The calculation of accurate free energies for protonation reactions is difficult due to the poor description of the solvation energy of protons by implicit solvent models. Therefore, the experimental value based on the Sackur-Tetrode equation and an estimated solvation energy of $G_{solv}(H^+) = -264.6$ kcal/mol in acetonitrile was used.[97,98] Studies found deviations of this approach versus experimental values of $\pm$ 3 pK_A units.[99] We tested our computational protocol for phenol: B3LYP yielded a pK_a of 24.8 and ωB97X-D 24.6 which are 4-5 units lower than the experimental value of 29.1 in acetonitrile.[100] In spite of this systematic com-

putational error, calculated relative pK_a values are more reliable because of favorable error cancellation by removing the experimental free energy of the proton. Thus, calculated pK_a values should mainly be compared against each other. It is important to point out that the implicit solvation model corresponds to a pure solution of acetonitrile. However, electrolysis experiments were conducted in a solution of 3 M phenol in acetonitrile, saturated with 1 atm of CO_2, not in pure acetonitrile. Therefore, the actual pK_a of possible intermediates under the experimental conditions should be lower than the calculated values due to several factors: first, experimental pK_a values of acids in mixtures of acetonitrile and water are lower than in pure acetonitrile.[100,101] This decrease in pK_a is not accounted for by the implicit solvent model used in our calculations. Second, the introduction of CO_2 to the water-acetonitrile-phenol mixture lowers the effective pK_a of the solution. This occurs via the direct formation of carbonic acid or complexation between CO_2 and OH^-. For reference, the experimental pK_a of water-acetonitrile mixtures saturated with carbon dioxide is estimated to be 11.[102] Therefore, we report not only the pK_a value of the protonation steps but also the free energy of the protonation reaction coupled to carbonic acid. This is in line with experimental approaches of determining the overpotential which also use carbonic acid as the proton source. Even if it is assumed that phenol is involved in the rate limiting barriers (*vide supra*), the conjugated base phenolate is reprotonated by the strongest acid in the solution which is carbonic acid or aqueous CO_2.[69]

We use phenol as the main proton source for calculating reaction barriers involving protonation reactions as it was added to the reaction mixture in the CPE experiments.[75] The concentration of other proton sources (H^+ and H_2CO_3) is negligible.[47] Nonetheless, we also present the reaction barriers with H_2CO_3 for the Fe system. These kinetic barriers do not reflect the experimental conditions. We include them here to illustrate how barriers for the protonation steps decrease with a stronger acid. The calculated pK_a in acetonitrile of H_2CO_3 (13) is significantly lower than phenol (25). We note that implicit solvation models poorly describe the solvation of anions where the charge is concentrated, e.g. PhO^-. The augmen-

tation of implicit solvent calculations with explicit water molecules improves the accuracy as it helps to account for strong short-range hydrogen bonding interactions between the anion and the solvent.[103] Hence, adding an explicit water molecule in the pK_a calculations to stabilize the conjugate base PhO^- decreases the pK_a to 22.

Reduction potentials are reported with an isodesmic scheme against the ferrocene/ferrocenium couple used as an internal standard.[104,105] This methods allows accurate predictions even at a modest level of theory with reported accuracy of $\sim$ 100 mV to experimental values.[105]

We used different functionals for the Fe (ωB97X-D) and Co (B3LYP) complexes as these functionals provided the best match between predicted and experimentally reported reduction potentials; see tables S2 and S3 in the supporting information (SI). Unfortunately, many properties[106] of transition metal systems like energetics of ligand dissociation,[107,108] adiabatic spin gaps (high spin–low spin)[109,110] or reduction potentials[111] are sensitive to limitations of approximate Kohn-Sham DFT functionals. In particular, many observables are quite sensitive to the amount of "exact" exchange (Hartee-Fock exchange), as this parameter strongly affects the extent to which the charge delocalization error (often also described as self-interaction error) affects a given system-functional pair.[112] Thus, a separate choice of functional for each transition metal complex was necessary to accurately reproduce the experimental findings. However, our main findings like relative barrier heights (see tables S4–S9), key MOs (see figure S19), localization of electrons upon reduction (ligand centered vs. metal centered; see figures S13–S18) and CO_2 binding modes (see figure S20 and S21) are robust to a broad spectrum of suitable functionals unless otherwise noted in the main text.

Results

We employ a naming scheme which encodes the spin multiplicity (2S+1), the total charge, the coordination number (CN), a consecutive number X for each intermediate step (1: initial

complex, 2: CO_2 adduct, ...) and an element symbol M (M = Co, Fe) to indicate the central metal: $^{\text{multiplicity}}[\mathbf{XM}(\text{CN})]^{\text{charge}}$ (see figure 2). As an example, $^{4}[\mathbf{1Co}(6)]^{2+}$ describes the initial hexacoordinated diaqua complex $[\text{Co}^{\text{II}}(\text{qpy})(\text{H}_2\text{O})_2]^{2+}$ in the quartet spin state and overall charge 2+.

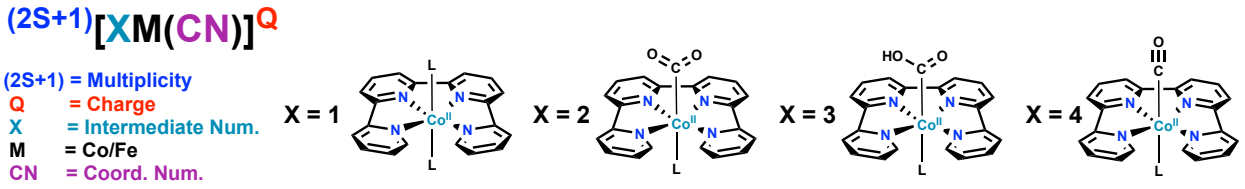

Figure 2: Naming scheme for intermediates used throughout the manuscript.

Catalytic Pathway for $[\text{Co}^{\text{II}}(\text{qpy})(\text{H}_2\text{O})_2]^{2+}$

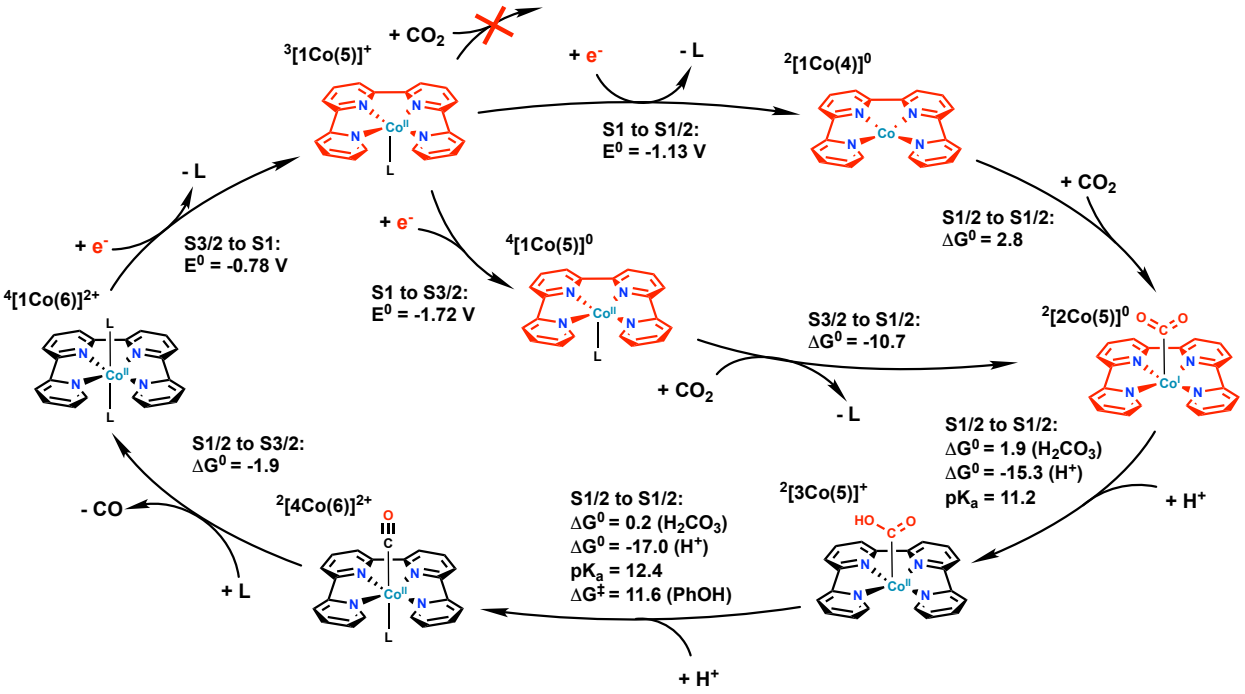

Figure 3: Proposed mechanism for the selective CO_2 to CO reduction using $[\text{Co}(\text{qpy})\text{L}_2]^{2+}$; the red colored molecular moiety indicates localization of the excess electrons; reaction and activation energies in kcal/mol; reduction potentials against Fc/Fc^{+}; L = H_2O; see figure 2 for the naming conventions.

The proposed catalytic cycle for the electrochemical reduction of CO_2 to CO with added

phenol (3 M) catalyzed by $[Co(qpy)(H_2O)_2]^{2+}$ is depicted in figure 3 (see figure S9 for a more detailed cycle including a possible third reduction). The first reduction of $[Co(qpy)(H_2O)_2]^{2+}$ ($^4[\mathbf{1Co}(6)]^{2+}$, figure 4 (a)) is a ligand based reduction in the low-lying π^* orbital of the non-innocent qpy moiety and accompanied by the loss of one aqua ligand forming $[Co(qpy)(H_2O)]^+$ ($^3[\mathbf{1Co}(5)]^+$). The reduction is further stabilized by an antiferromagnetic (afm) coupling to the high-spin d^7 Co(II) center, which rationalizes the low reduction potential. The electronic structure is illustrated with a schematic MO diagram in figure 6 (a). The calculated reduction potential is -0.78 V (vs Fc^+/Fc), which is in acceptable agreement with the experimentally measured potential (-0.95 V). The electronic structure is illustrated by the spin density plot of $^3[\mathbf{1Co}(5)]^+$ in figure 4 (c) and can be compared to the spin density of $^4[\mathbf{1Co}(6)]^{2+}$ in figure 4 (b) where the spin density is localized solely on the metal center. The ligand loss reduces the negative charge on the central metal and allows a stronger afm coupling. This seems to compensate for the weaker d orbital splitting, maintaining the high spin state.

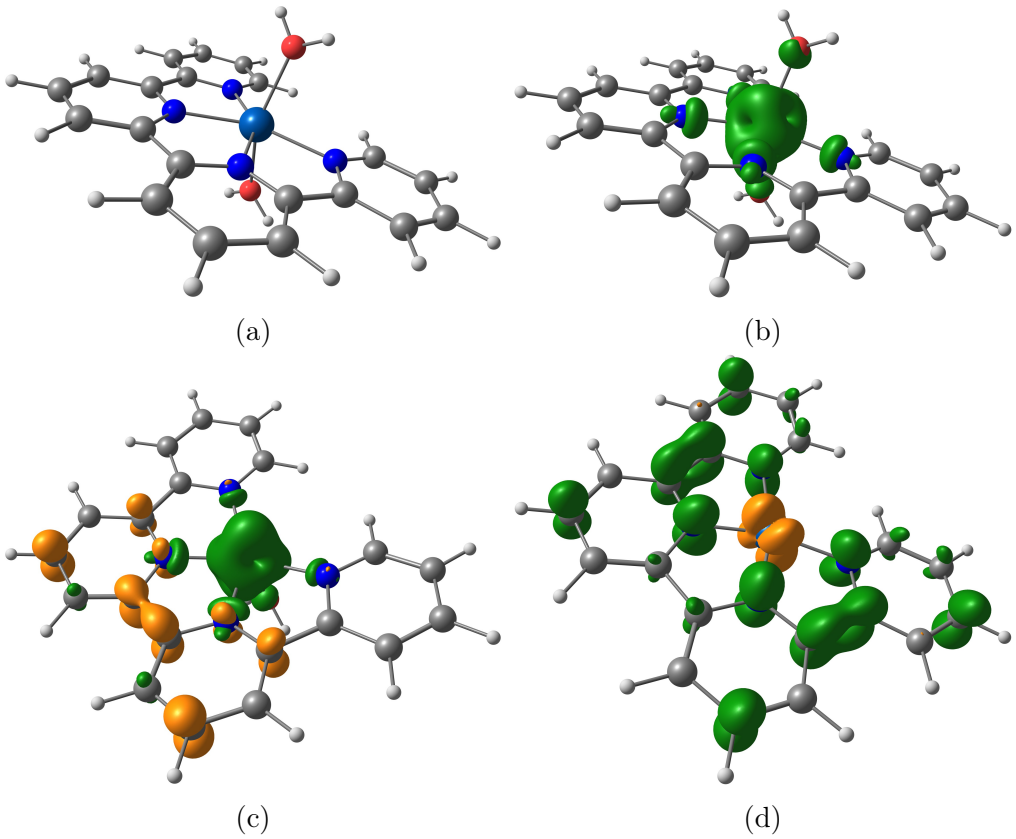

Figure 4: (a) Geometry of the unreduced $[Co^{II}(qpy)(H_2O)_2]^{2+}$ (^{4}[**1Co**(6)]$^{2+}$); (b) Spin density of ^{4}[**1Co**(6)]$^{2+}$; (c) Spin density of the singly reduced intermediate ^{3}[**1Co**(5)]$^{+}$; (d) Spin density of the doubly reduced intermediate ^{2}[**1Co**(4)]^{0}. Green and gold colors indicate excess of α or β spin electron density, respectively.

The second reduction step is accompanied by the dissociation of the second aqua ligand to form $[Co(qpy)]^0$ ($^2[\mathbf{1Co}(4)]^0$) with a distorted square planar coordination geometry. Counterintuitively, the weaker d orbital splitting accompanies a spin transition to a low spin Co resulting in a doublet metal center with a singly occupied d_{xz} type orbital and an empty $d_{x^2-y^2}$. This surprising result can be explained by a bonding interaction between the metal and qpy ligand, which stabilizes the second excess electron. The bonding occurs due to the stabilization of the d_{xz} orbital by coupling with the qpy π^* orbital. Analysis of the electronic structure reveals that the second excess electron is strongly delocalized between metal and ligand. It can be understood as a formally doubly reduced qpy moiety (triplet π^*) and a doublet Co^{II} (d_{xz}) coupling to an overall doublet with a weak π type metal ligand bond. The HOMO in the α space is a solely qpy based π^*, but the HOMO-1 exhibits significant metal contribution (46%) and a π type bonding character between the d_{yz} (which is empty in the α space) and a qpy π^*. The electronic structure is illustrated in a schematic MO diagram in figure 6 (b) and the spin density plot in figure 4 (d). Thus, the second electron is highly delocalized between the metal and the qpy moiety and the reduction *cannot* be classified as metal or ligand based. Further evidence for the significant metal contribution in the second reduction is shown by the comparison of the doublet $^2[\mathbf{1Co}(4)]^0$ to the corresponding quartet $^4[\mathbf{1Co}(4)]^0$ (uncoupled metal doublet and ligand triplet), which localizes both excess electrons in the qpy ligand. The partial Mulliken charges on Co change by 0.4 from the quartet state to the doublet state. (The spin contamination of this broken symmetry solution is mild ($\langle S^2 \rangle$ =0.92) which also confirms small contributions of the quartet spin state and a bonding character between the Co d_{xz} and qpy π^*). Thus, the energetics and overlap of Co d_{xz} and qpy π^* allows for an efficient delocalization of the electron over both metal and ligand. The formation of this bonding interaction significantly shortens Co-N bond distances to 1.93 Å (from 2.14 Å in $^3[\mathbf{1Co}(5)]^+$) which results in a distortion of the qpy framework to avoid repulsion of two hydrogen atoms (see figure S1 (b)). In contrast, the first reduction from $^4[\mathbf{1Co}(6)]^{2+}$ to $^3[\mathbf{1Co}(5)]^+$ does not change the bond distance significantly (2.16 to 2.14 Å).

The stabilization of the second excess electron via the metal-ligand bond rationalizes the mild second reduction potential. The calculated reduction potential is -1.13 V (vs Fc/Fc^+), which is in excellent agreement with the experimentally measured potential (-1.18 V). It is noteworthy that a ligand centered first reduction was also observed in all other possible spin states; furthermore, these findings are robust with respect to different DFT functionals (for all possible spin states as well). The doubly reduced doublet species ($^2[\mathbf{1Co}(4)]^0$) was also identified as the most stable isomer among all possible doubly reduced isomers, but the degree of metal-ligand delocalization varied among different density functionals (see table S1). However, the metal-ligand delocalization observed with the B3LYP functional is similar to multi-reference active space (CASSCF) calculations (see table S1 and SI section CASSCF).

Experimentally, the first reduction wave is reversible, but the second one is irreversible and only visible at slow scan rates. Because of this, Robert *et al.*[75] assign the first reduction to be metal centered and the second reduction as ligand centered, with a slow loss of H_2O which was also hypothesized by Che *et al.*[74] This is in contrast to our calculations, in which the first reduction is mainly ligand based and the loss of the first aqua ligand does not change the spin at the Co center. Thus, the reorganization energy is small, and the electron transfer is fast. In contrast, the second reduction has significant metal character and also induces a spin transition from high spin to low spin. Consequently, the reorganization energy is significantly larger and the kinetics of the electron transfer more sluggish. Thus, we provide an alternative interpretation of the experimental observations. Further CV experiments with phenol revealed a binding of phenol to the complex after the first reduction and a significant shift in the second reduction wave to -1.66 V vs Fc^+/Fc (from -1.18 V). This can be compared to the calculated reduction potential of the second reduction *without* an allowed water loss: -1.72 V vs Fc^+/Fc from $^3[\mathbf{1Co}(5)]^+$ to $^4[\mathbf{1Co}(5)]^0$ (assuming the effect of H_2O and PhOH on the d orbital splitting is similar). This highlights the importance of the ligand loss and the spin transition in order to access the stable doubly reduced intermediate

^{2}[**1Co**(4)]^0.

It is noteworthy that a similar reduction pathway was observed by some of us with experimental evidence for the reduced intermediates in an iron complex with a terpyridine ligand scaffold.[37] Both reductions are ligand based, but the second reduction is accompanied by the loss of an acetonitrile ligand and a spin transition from a low spin to intermediate spin iron (S = 2). The metal d orbital mixes strongly with the terpyridine π^* orbitals, similarly resulting in a mild reduction potential. The π^* orbitals of the qpy moiety are even lower in energy than the terpyridine moiety, which rationalizes that these orbitals are involved in both reduction steps of $[Co(qpy)(H_2O)_2]^{2+}$.

The catalyst state which binds CO_2 is most likely the doubly reduced complex ^{2}[**1Co**(4)]^0 (or ^{4}[**1Co**(5)]^0) because it was not possible to converge a singly reduced CO_2 adduct. This suggests that the catalytic pathway follows an EEC mechanism. CO_2 binds to ^{2}[**1Co**(4)]^0 in the η^1-κC binding mode to form $[Co(qpy)(CO_2{-}\kappa C)]^0$ (^{2}[**2Co**(5)]^0) and the binding induces bending of the CO_2 $\angle$(OCO) angle of 146°, which indicates the transfer of nearly one electron into the CO_2 moiety as the $\angle$(OCO) is 134° for free $CO_2^{\cdot-}$ (see figure 7 (a)). It was not possible to obtain either an η^2 or η^1-κO isomer. The spin density plot of ^{2}[**2Co**(5)]^0 shows little spin polarization on both Co and CO_2 and one electron still occupies the qpy π^* (see figure 7 (b)). This is also confirmed by the Mulliken spin population which is approximately 0.2 for both Co and CO_2. Analysis of the MOs suggests a Co(I) in a d^8 configuration forming a dative σ bond with CO_2 via the doubly occupied d_{z^2} and the CO_2-LUMO, see figure 6 (c). The hybrid d_{z^2} + CO_2-π^* MO has $\sim$ 70% d_{z^2} character. The oxidation state is confirmed by a localized orbital bonding analysis[113] which localizes 3 orbitals with over 90% Co d-character and one d orbital with over 70% Co d-character. The binding is slightly endergonic but barrierless (ΔG = 2.8 kcal/mol). The lowered oxidation state makes Co a good Lewis base, and the low coordination number stabilizes the d_{z^2} orbital; both factors seem to facilitate CO_2 binding. We probed the effect of adding a single explicit water to stabilize the reduced CO_2 in ^{2}[**2Co**(5)]^0. The structure is depicted in S2 (a) and shows a

more activated CO_2 as the $\angle$(OCO) slightly decreases. However, the stabilizing effect on thermodynamics is small as the formation of this complex is thermodynamically neutral. The CO_2 addition becomes significantly more exergonic (-10.7 kcal/mol) under higher acid concentration and a more negative potential for CPE as this implies a pathway via the less stable doubly reduced $^4[\mathbf{1Co}(4)]^0$. This is in line with the experimental finding that a potential of -1.5 V vs Fc/Fc^+ is required to observe significant catalysis. Our calculation suggest that additional thermodynamic driving force is necessary as the subsequent reaction steps (protonation) are endergonic (*vide infra*).

The subsequent protonation of the CO_2 adduct $^2[\mathbf{2Co}(5)]^0$ is also barrierless using PhOH as the proton source with a pK_a of 11 and is slightly endergonic coupled to the deprotonation of H_2CO_3 (1.9 kcal/mol). Upon proton transfer, both excess electrons localize on the CO_2 moiety as the CO_2 angle of 121° indicates (see figure 8 (a)). The resulting anionic carboxy intermediate $[Co(qpy)(COOH)]^+$ ($^2[\mathbf{3Co}(5)]^+$) is stabilized by a dative bond to a low spin Co(II) central metal. Thus, the addition of a proton source leads to the second reduction of CO_2 via a push-pull mechanism, where the initial reduction of CO_2 is achieved by a "push" from the metal center and the second reduction arises from "pulling" of the acid associated with the first protonation.[114] If phenol is assumed to be the proton source, the catalytic cycle proceeds most likely via a phenoxide–$^2[\mathbf{3Co}(5)]^+$ complex. The phenoxide is then either reprotonated via the reaction with water and CO_2 yielding phenol and HCO_3^- or stabilized by a counter-ion (e.g. electrolyte). The free energy for the formation of this complex is estimated to be 10.6 kcal/mol (see figure S3). Hence, this reaction step could become slow during long electrolysis experiments when the pH of the reaction increases as the concentration of CO_2 decreases.

The second protonation yields the carbonyl intermediate $[Co(qpy)(H_2O)(CO)]^{2+}$ ($^2[\mathbf{4Co}(6)]^{2+}$) and water with a pK_a of 12 which is thermodynamically neutral when coupled to the deprotonation of H_2CO_3 (0.2 kcal/mol). The protonation process is coupled to the C$-$O bond cleavage; the transition state exhibits a stretched C$-$O bond (2.12 Å) and is depicted in fig-

ure 8. The activation barrier for the reaction is 11.6 kcal/mol, constituting the rate limiting step in the cycle (corresponding to a rate of $\sim$20000 s^{-1}). $^{2}[\mathbf{4Co}(6)]^{2+}$ is not stable since the high oxidation state of the central metal allows only for a weak backbonding interaction with CO. Consequently, the dissociation of CO and regeneration of $[Co(qpy)(H_2O)_2]^{2+}$ is thermodynamically favorable ($\Delta_R G = -1.9$ kcal/mol). In total, the pathway via $^{2}[\mathbf{1Co}(4)]^{0}$ exhibits three consecutive endergonic reaction steps and is overall endergonic by 3 kcal/mol. This could explain why no catalysis is observed at -1.13 V vs Fc/Fc^{+}. Instead at higher acid concentration and more negative potential the less stable doubly reduced intermediate $^{4}[\mathbf{1Co}(5)]^{0}$ is accessed which makes CO_2 addition, and the whole pathway, exergonic.

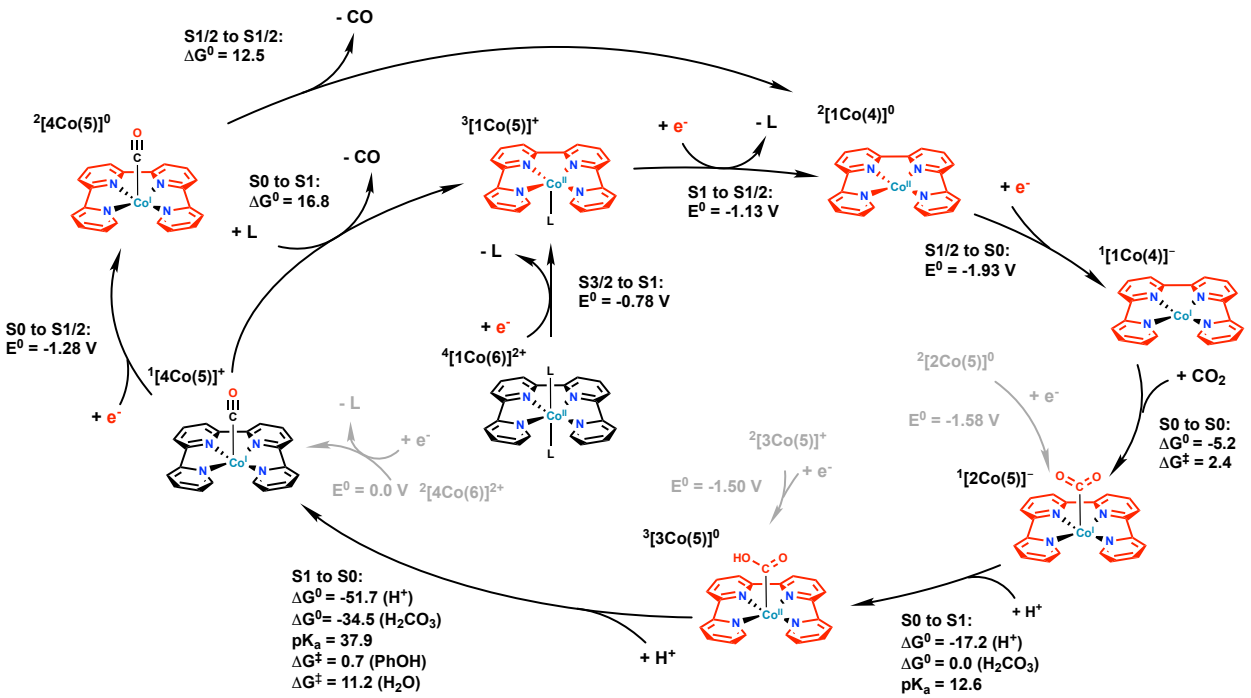

Figure 5: Proposed mechanism for CO_2 to CO reduction using $[Co(qpy)L_2]^{2+}$ and incorporating a third reduction; the red colored molecular moiety indicates localization of the excess electrons; reaction and activation energies in kcal/mol; reduction potentials against Fc/Fc^+; L = H_2O; grey arrows indicate connections (via reduction) to doubly reduced intermediates (see figure S9 for the full cycle); see figure 2 for the naming conventions.

Increasing the applied potential to −1.98 V vs Fc^+/Fc enables CO_2 reduction at lower acid concentrations (0.1 M PhOH), albeit with a lower selectivity since a significant amount of H_2 is produced as well (*vide infra*).[76] A possible mechanism at this more negative applied potential is depicted in figure 5. The third reduction of the initial complex leads to $^1[\mathbf{1Co}(4)]^-$ in a singlet ground state with a doubly reduced qpy ligand (in the same orbital) and a d^8 Co(I) center. The computed reduction potential is −1.93 V vs Fc/Fc^+, which is in excellent agreement with the experimentally[76] predicted reduction potential (−1.89 V vs Fc/Fc^+). The subsequent CO_2 addition is exergonic (−5.2 kcal/mol) and has a small barrier of 2.4 kcal/mol. The adduct binds CO_2 also in a κC binding mode ($^1[\mathbf{2Co}(5)]^-$). This suggests an EEEC mechanism for CO_2 binding. The subsequent first protonation yielding $^3[\mathbf{3Co}(5)]^0$ is barrierless and thermodynamically neutral when coupled to deprotonation of H_2CO_3 with a pK_a of 13. The second protonation yielding the carbonyl complex, $^1[\mathbf{4Co}(5)]^+$, is barrierless

(0.7 kcal/mol) using phenol as the proton source. The process is strongly exergonic with a pK_a of 38 and free energy of −34.5 kcal/mol (when coupled to deprotonation of H_2CO_3). The barrier remains low (11.2 kcal/mol) even with water as the proton source which explains the experimentally observed high activity without the addition of a proton source or at low phenol concentrations. In this case the main proton source is most likely water. The driving force for the second protonation is the very stable singly reduced carbonyl which entails an extremely endergonic CO release (16.8 kcal/mol) to regenerate $^3[\mathbf{1Co}(5)]^+$. Thus, the CO release is slow, the rate limiting step in this alternative pathway and $^1[\mathbf{4Co}(5)]^+$ a persistent intermediate. The carbonyl $^1[\mathbf{4Co}(5)]^+$ is likely to accumulate during catalysis which increases the possibility for a further reduction to $^2[\mathbf{4Co}(5)]^0$ at −1.28 V vs Fc/Fc^+. Then, the regeneration of the catalyst is significantly less exergonic (12.5 kcal/mol). In addition, the low solubility of CO and the negative applied potential should further shift the equilibrium and facilitate the release.

In summary, an alternative pathway involving a third (and fourth reduction) is able to drive CO_2 reduction at a lower acid concentration (0.1 M versus 3 M) but a higher applied potential (1.98 V versus 1.5 V vs Fc/Fc^+). The second protonation and the CO release are the rate limiting processes. The stability of the carbonyl intermediate allows to drive the reaction efficiently even with water as the proton source (see figure S11(a)–(c) for the transition states). Therefore, this catalyst is able to operate efficiently under different experimental conditions by proceeding via a second mechanism. In both proposed cycles, the rate-limiting barriers are similar which is in line with the similar experimentally measured rates despite the distinct conditions.[75,76]

A connection to the third reduction pathway is accessible at all intermediates as the reduction of the CO_2, CO_2H and CO intermediates is possible at potentials lower than −1.72 V vs Fc/Fc^+ (the second reduction at high acid concentration, see figure S9 for a detailed cycle including a third reduction for every intermediate). Thus, triply reduced intermediates could accumulate and could be responsible for the generation of H_2 as the

selectivity in the three electron pathway is significantly lower. However, the first protonation process is barrierless, the barrier for the second protonation barrier is low and the CO release is barrierless. Therefore, it is unlikely for both $^2[\mathbf{4Co}(6)]^{2+}$ and $^2[\mathbf{3Co}(5)]^{+}$ to persist long enough in order to get further reduced. This is also in line with experimental observations as FE for CO_2 to CO conversion is 94%.

A possible HER mechanism is depicted in figure S7, starting with a direct protonation of $^2[\mathbf{1Co}(4)]^0$. The formation of a hydride has a pK_a of 12 similarly to both protonation steps in the CO2RR cycle and is thermodynamically neutral (0.2 kcal/mol). However, it was not possible to find a transition state for the direct formation of a hydride with phenol. The acid prefers to coordinate to the metal via a dative bond (via O) which can lead to a possible protonation of a pyridine. This could either be a possible degradation pathway or HER proceeds via an unconventional pathway which is most likely not competitive with the barrierless CO_2 addition. This is in line with experimental findings as CPE experiments with the addition of phenol yield over 96% CO. The exact nature of the (minority) HER mechanism, however, is beyond the scope of this work. The formation of a hydride after three reductions via $^1[\mathbf{1Co}(4)]^-$ is exergonic with a pK_a of 18 and -7.3 kcal/mol. Furthermore, the process is barrierless (using phenol as the proton source) which can explain the significant amount of H_2 produced by this pathway.

The in-depth analysis of possible catalytic pathways is a basis for modifications to improve the catalyst by optimizing the metal-ligand interaction for $^2[\mathbf{1Co}(4)]^0$. Performance could be altered by modifying the energy of the qpy π^* orbitals by introducing electron donating or withdrawing substituents. Table 1 shows the effect of three substituents ($-NH_2$, $-F$, $-CN$) on both the reduction potentials and the barrier of the (rate limiting) transition state. We assume that the introduction of the substituents do not alter the proposed mechanism. The substituent is introduced twice at the 4″ and 4‴ positions (para positions of the two inner pyridines). We probe both a positive mesomeric effect with $-NH_2$ and a negative mesomeric effect with $-CN$. The amino group raises the qpy π^* orbital energy and this

consequently increases the reduction potentials significantly. Conversely, the nitrile group lowers the qpy π^* orbital energy which reduces the reduction potentials. The first reduction is more affected since it is mainly ligand based. The effect on the barriers is reversed: the amino group decreases the barrier whereas the nitrile increases the barrier. Interestingly, the fluoride group has a weak positive mesomeric effect and negative inductive effect which decreases both overpotential and the barrier mildly. Furthermore, a fluoride substituent would increase the solubility in aqueous solutions.

The amino-qpy could both decrease overpotential and increase catalytic activity more significantly by altering the pathway. The analysis of the unsubstituted complex's catalytic pathway suggested that the less stable doubly reduced $^4[\mathbf{1Co}(5)]^0$ is accessed under high acid concentrations and higher applied potentials as these conditions provide important thermodynamic driving forces for the subsequent reaction steps (*vide infra*). In case of the amino-qpy, the increase of the second reduction potential could provide enough thermodynamic driving force to drive catalysis via the four coordinated doubly reduced intermediate $^3[\mathbf{1Co}(4)]^0$ at less negative potential than the unsubstituted complex (via $^4[\mathbf{1Co}(5)]^0$). In addition, the amino substituent decreases the barrier of the rate limiting step substantially. Hence, the amino group could reduce both the overpotential and increase the rate.

Table 1: Effect of introducing a substituent at the 4″ and 4‴ position of the qpy on both reduction potentials and the barrier of the second protonation (rate limiting step). Reduction potential in V versus Fc/Fc^+, activation energy in kcal/mol using phenol as the proton source.

Substituent	E_1	E_2	$\Delta G^{\ddagger}$
−H	−0.78	−1.13	11.6
$-NH_2$	−1.11	−1.31	7.9
−CN	−0.24	−0.79	17.7
−F	−0.71	−1.08	10.9

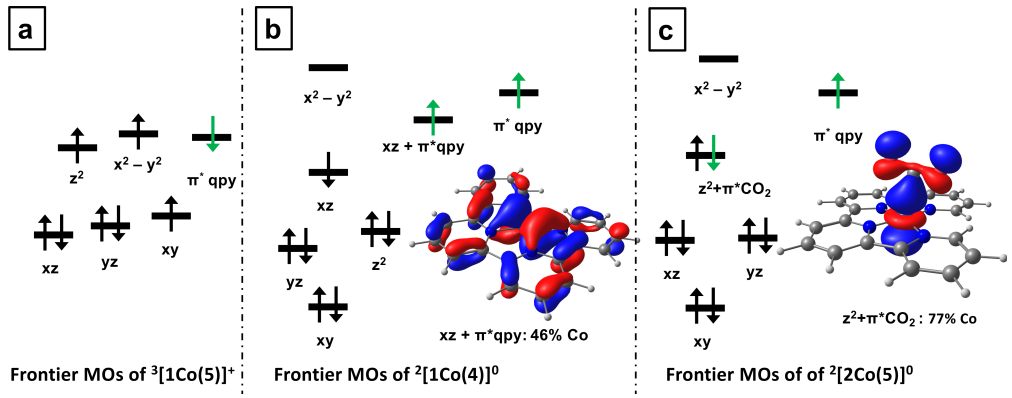

Figure 6: Schematic MO diagram of the important intermediates in the cycle: a) the singly reduced complex $[Co(qpy)(H_2O)]^+$ ($^3[\mathbf{1Co}(5)]^+$), b) the doubly reduced complex $[Co(qpy)]^0$ ($^2[\mathbf{1Co}(4)]^0$) and c) the CO_2 adduct $[Co(qpy)(CO_2{-}\kappa C)]^0$ ($^2[\mathbf{2Co}(5)]^0$). The green arrows indicate the extra electrons due to reduction. The MO in (b) illustrates the delocalized π type metal (d_{xz}) ligand (π^*) bond to stabilize the excess electron; the MO in panel (c) illustrates the σ type interaction of the Co-d_{z^2} orbital and the CO_2 LUMO leading to the η^1 binding mode in $[Co(qpy)(CO_2{-}\kappa C)]^0$.

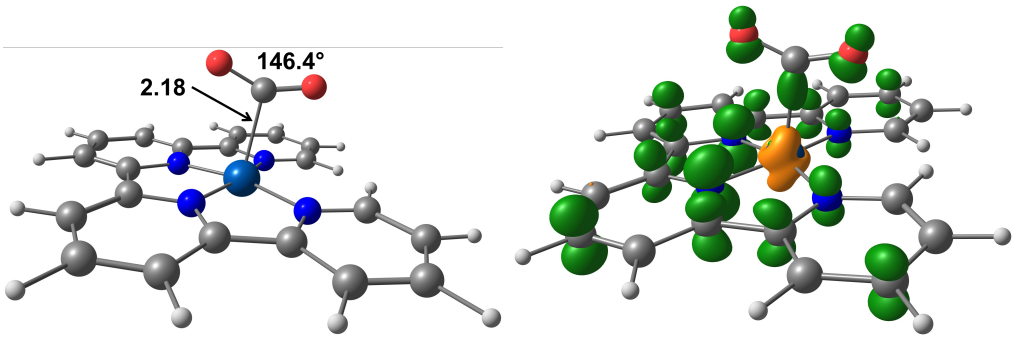

(a) (b)

Figure 7: (a) Geometrical parameters of $[Co(qpy)(CO_2)]^0$ ($^2[\mathbf{2Co}(5)]^0$), the doubly reduced complex that binds CO_2, with emphasis on the structural features of the CO_2 ligand; (b) Spin density of the complex, showing most spin density remains on the qpy ligand.

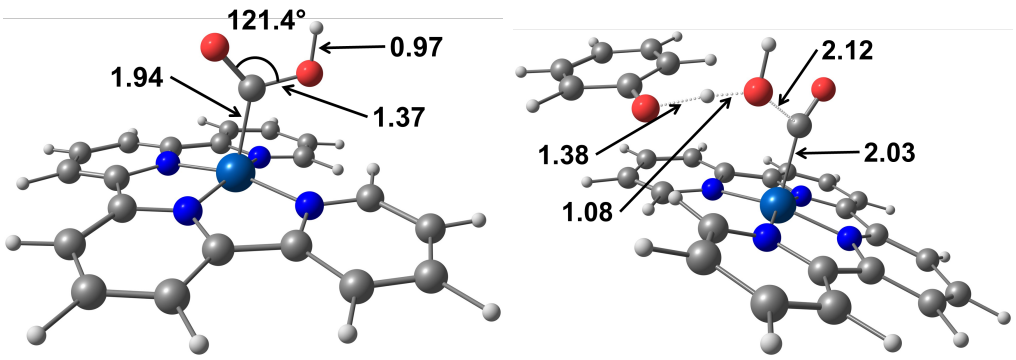

(a) (b)

Figure 8: (a) Geometrical parameters pertaining to $[Co(qpy)(CO_2H)]^+$ (^{2}[**3Co**(5)]$^+$), highlighting the CO_2H ligand and (b) transition state for the second protonation step of $[Co(qpy)(CO_2H)]$, with phenol as the proton donor, emphasizing the structural changes of the involved species.

Catalytic Pathway for $[Fe^{II}(qpy)(H_2O)_2]^{2+}$

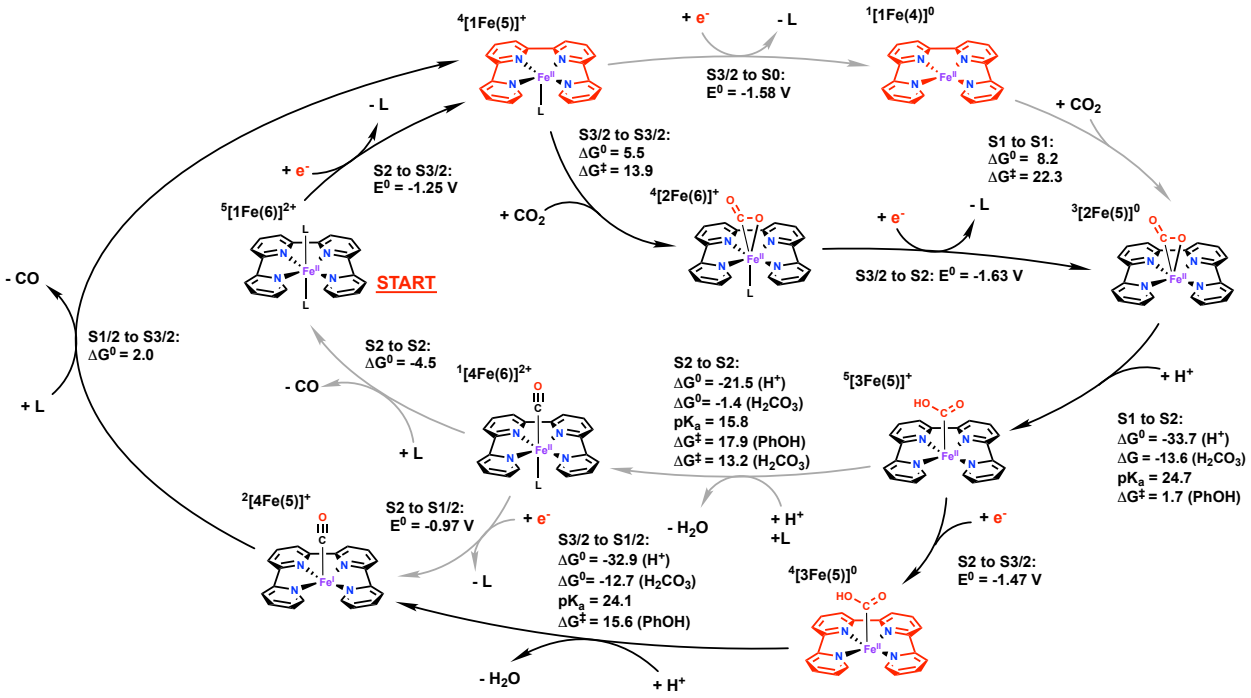

Figure 9: Proposed mechanism for the selective CO_2 to CO reduction using $[Fe(qpy)L_2]^{2+}$; the red colored molecular moiety indicates localization of the excess electrons; grey arrows indicate alternative competitive pathways; reaction and activation energies in kcal/mol; reduction potentials against Fc/Fc^+; L = H_2O; see figure 2 for the naming conventions.

The proposed catalytic cycle for the electrochemical reduction of CO_2 using $[Fe^{II}(qpy)(H_2O)_2]^{2+}$ is depicted in figure 9 (a more detailed cycle including a possible third reduction at every intermediate step can be found in figure S10). The initial first reduction of $[Fe(qpy)(H_2O)_2]^{2+}$ (^{5}[**1Fe**(6)]$^{2+}$) to $[Fe(qpy)(H_2O)]^+$ (^{4}[**1Fe**(5)]$^+$) is a ligand based reduction in the low-lying π^* orbital of the non-innocent qpy moiety which is accompanied by the loss of one aqua ligand (see figure 10 (a)). The electronic structure is illustrated by the spin density plot of ^{4}[**1Fe**(5)]$^+$ in figure 10 (c) which exhibits an unpaired electron in the π^* of the qpy ligand framework antiferromagnetically coupled to the high spin metal (in contrast to the spin density of ^{5}[**1Fe**(6)]$^{2+}$ in figure 10 (b)). The electronic structure is illustrated by the schematic MO diagram in figure 11 (a). The calculated reduction potential is -1.25 V vs Fc/Fc^+ which is in good agreement with the experimentally measured potential (-1.39 V) but slightly less

negative. This could suggest that the DFT calculation slightly overestimate the stabilization by the afm coupling. It is noteworthy that the potential of the solely ligand based reduction to the (uncoupled) sextet is −1.41 V, which is in even better agreement with the experimental potential.

The second reduction is also accompanied by a ligand loss to form $[Fe(qpy)]^0$ ($^1[\mathbf{1Fe}(4)]^0$). The square planar coordination geometry induces a spin transition on the Fe(II) from high spin (S = 2) to intermediate spin (S = 1). Unlike the cobalt catalyst, the second reduction is ligand based in a second qpy π^* orbital. The Fe contribution to both qpy π^* orbitals is small (5% & 11%). The electronic structure is best described as intermediate spin triplet Fe(II) coupled to a triplet doubly reduced qpy ligand. The electronic structure is illustrated by the spin density in figure 10 (d) and a schematic MO-scheme in figure 11 (b). This is also confirmed by CASSCF calculations as the metal ligand bonding is weaker in $^1[\mathbf{1Fe}(4)]^0$ in comparison to $^2[\mathbf{1Co}(4)]^0$ (see SI section CASSCF). The computed reduction potential of −1.58 V vs Fc/Fc^+ is in very good agreement with the experimentally measured potential (−1.60 V[75]). It is noteworthy, that ligand based reductions were also observed in all other possible spin states for both reduction events. Furthermore, these findings are robust with respect to different exchange-correlation functionals (see figures S16–S18).

Experimentally both reduction potentials are reversible with fast kinetics which suggests minimal structural reorganization. Our computational results show that both reductions are ligand based with little mixing between the iron d orbitals and qpy π^* which could explain the fast kinetics of both reductions. Hence, the Fe d orbitals are not suited to mix strongly with the π^* orbitals yielding ligand centered reductions.

The subsequent CO_2 binding is possible after either a single reduction event yielding the CO_2 adduct $[Fe(qpy)(H_2O)(\eta^2{-}CO_2)]^+$ ($^4[\mathbf{2Fe}(6)]^+$) or after two reduction events yielding $[Fe(qpy)(\eta^2{-}CO_2)]^0$ ($^3[\mathbf{2Fe}(5)]^0$). In both cases CO_2 binds in an η^2 binding mode; no η^1-κC isomer could be located as a minimum structure, and the η^1-κO isomers were significantly higher in energy (first reduction: ∼6 kcal/mol and second reduction: ∼13 kcal/mol). The

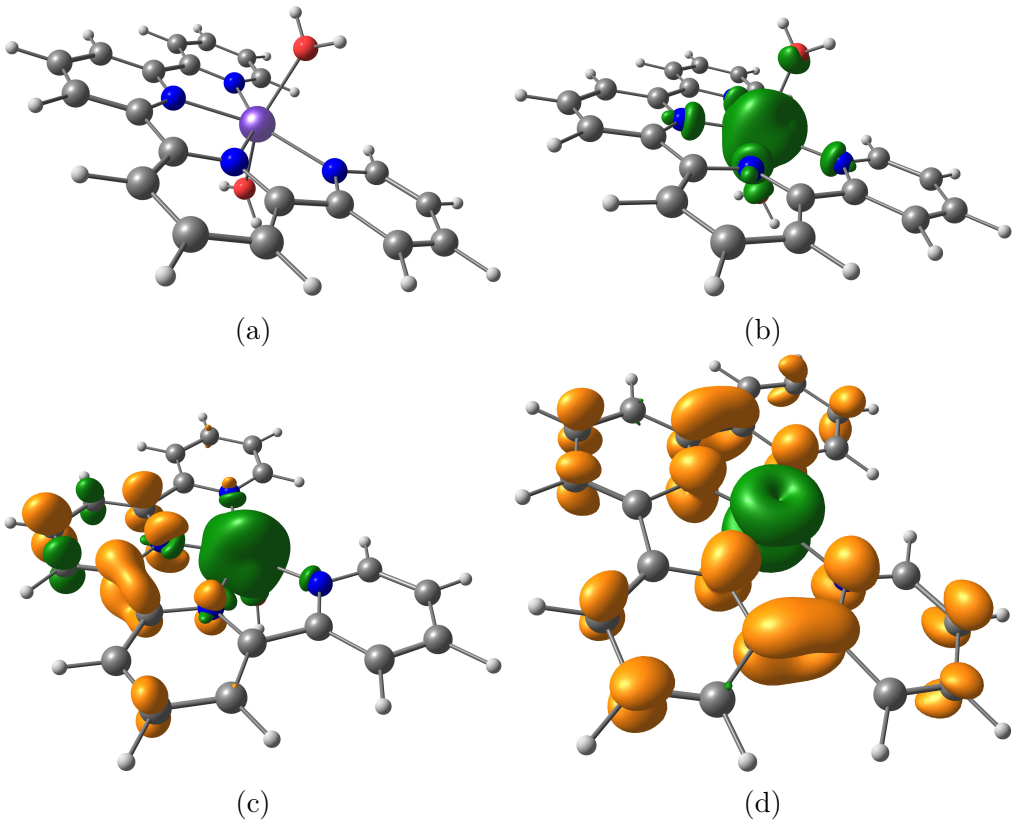

Figure 10: (a) Geometry of the unreduced $[Fe^{II}(qpy)(H_2O)_2]^{2+}$ (^{5}[**1Fe**(6)]$^{2+}$); (b) Spin density of ^{5}[**1Fe**(6)]$^{2+}$; (c) Spin density of the singly reduced intermediate ^{4}[**1Fe**(5)]$^{+}$; (d) Spin density of the doubly reduced intermediate ^{1}[**1Fe**(4)]^{0}. Green and gold colors indicate excess of α or β spin electron density, respectively.

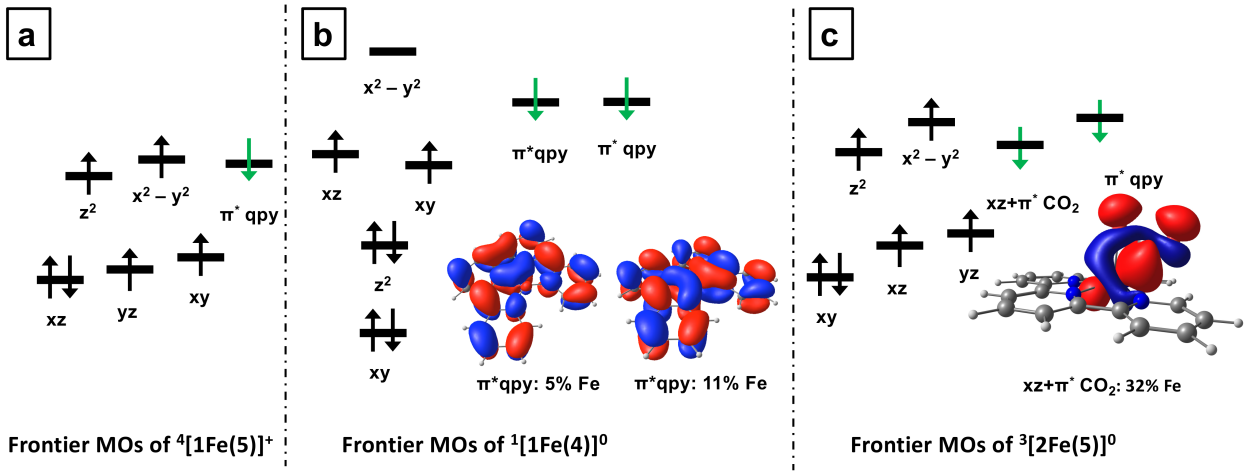

Figure 11: Schematic MO diagram of the important intermediates in the cycle: a) the singly reduced complex $[Fe(qpy)(H_2O)]^+$ (^{4}[**1Fe**(5)]^0), b) the doubly reduced complex $[Fe(qpy)]^0$ (^{1}[**1Co**(4)]^0) and c) the CO_2 adduct $[Fe(qpy)(\eta^2{-}CO_2)]^0$ (^{3}[**2Fe**(5)]^0). The green arrows indicate the extra electrons due reduction. The MOs in (b) illustrate the mainly ligand based character of the two reductions; the MO in panel (c) illustrate the π type CO_2 LUMO Fe-d_{yz} bond in $[Fe(qpy)(\eta^2{-}CO_2)]^0$.

binding of CO_2 induces a bending of the CO_2 angle to 147°, and the Fe−O bond distance is slightly elongated in comparison to the Fe−C bond (see figure 12 (a) & (c)).

The electronic structure analysis of ^{4}[**2Fe**(6)]$^+$ reveals a high spin (quartet) Fe center and a singly reduced $CO_2^{\cdot-}$ radical moiety (see figure 12 (b)). This indicates a charge transfer from the π^* orbital of the qpy into the π^* orbital of the CO_2 upon binding. The $CO_2^{\cdot-}$ moiety is stabilized by two pathways: first, by delocalizing some electron density from the CO_2-π^* into the unoccupied (in the β-space) Fe-d_{xz} via a π-type metal ligand bond; second, by a dative bond of the oxygen lone pair. This bonding situation is illustrated in the MO scheme in figure 11 (c) (see also figure 17 (b) for the MO of the dative bond). Furthermore, this binding mode was also observed both experimentally for a nickel complex[115] and in a computational study of a similar iron based catalyst by some of us.[71] The η^2 binding mode benefits from a Lewis acidic metal center due to the additional dative bond from the CO_2-oxygen and is able to stabilize the $CO_2^{\cdot-}$ moiety after a single reduction event. By contrast, iron-porphyrin based catalysts are only able to form a CO_2 adduct after multiple

reductions.[35,69]

The electronic structure of the doubly reduced CO_2 adduct ^{3}[**2Fe**(5)]^0 is similar to the singly reduced ^{4}[**2Fe**(6)]$^+$ –high spin Fe center and stabilized $CO_2^{\cdot -}$ moiety– as indicated by the similar O−C−O angle, Fe−C and Fe−O bond distances (see figure 12 (c)). The second excess electron is localized in the qpy ligand framework, and stabilized by afm coupling. Interestingly, the afm coupling to the reduced qpy ligand moiety decreases the Lewis-acidity of the Fe center. This weakens the dative bond from the CO_2 oxygen lone pair illustrated by the elongation of the Fe−O bond from 2.19 Å in ^{4}[**2Fe**(6)]$^+$ to 2.25 Å in ^{3}[**2Fe**(5)]^0 despite the loss of the water ligand. We gauged the effect of adding an explicit water to stabilize the activated CO_2 for both CO_2 adducts (see figures S2 (b) and (c)). The effect is similar in both cases: the CO_2 angle decreases further indicating a more activated CO_2 moiety.

The existence of a stable singly and doubly reduced CO_2 adduct yields two conceivable pathways: either reduction-CO_2-binding-reduction (ECE mechanism) or reduction-reduction-CO_2 binding (EEC mechanism). The binding of CO_2 is thermodynamically more favorable after the first reduction (5.5 kcal/mol versus 8.2 kcal/mol) but endergonic in both cases. However, binding after a single reduction (ECE) overcomes a significantly lower barrier (by 8.4 kcal/mol) which translates to a reaction rate that is seven orders of magnitude faster. Both transition states show similar levels of CO_2 activation with an O−C−O angle of 157° and a Fe−C bond distance of 2.3 Å. The weaker dative bond for the doubly reduced adduct ^{3}[**2Fe**(5)]^0 translates also to the TS: the key difference is the much shorter Fe−O bond distance in the transition state after a single reduction (see figures 13 (a) & (b)) and could explain the lower barrier after a single reduction. The free energy for CO_2 binding is most likely lower than the reported one due to the overestimation of the calculated entropic contribution of CO_2 (see the Computational Model section). The computed reduction potential of ^{4}[**2Fe**(6)]$^+$ to ^{3}[**2Fe**(5)]^0 is −1.63 V. This is 0.05 V higher than the predicted second reduction of the initial complex **1Fe** and should therefore be accessible.

Hence, CO_2 binding most likely occurs after a single reduction event (ECE mechanism).

This is in line with experimental findings as CV experiments under CO_2 atmosphere lead to a positive shift and loss of reversibility in the first reduction wave. This suggests a chemical reaction step after the first reduction. Scan rate dependence studies showed a rate constant of 82 $s^{-1}M^{-1}$ which corresponds to a barrier of ∼15 kcal/mol similar to the computed barrier of 13.9 kcal/mol.

The subsequent protonation of the CO_2 adduct ^{3}[**2Fe**(5)]^0 yields the carboxy adduct [Fe(qpy)(COOH)]$^+$ (^{5}[**3Fe**(5)]$^+$), the protonation of the singly reduced adduct ^{4}[**2Fe**(6)]$^+$ is thermodynamically unfavorable. The protonation induces charge transfer of the second excess electron from the qpy π^* orbital into the CO_2H moiety which also causes a change in the binding mode from η^2 to η^1-κC and decreases the O−C−O binding angle to 118°. The spin density is localized solely on the Fe-center which implies a doubly reduced CO_2H^- moiety acting as a ligand through the carbon lone pair to a high spin Fe center. The reaction is thermodynamically favorable by −13.6 kcal/mol (coupled to H_2CO_3) as indicated by the high pK_a (25), where the main driving force is to restore aromaticity in the qpy ligand. The activation energy of 1.7 kcal/mol makes this process almost barrierless; the transition state is depicted in figure 14 (b). The addition of a water molecule is essential to facilitate a fast protonation step. In the transition state a water molecule significantly facilitates the protonation as it stabilizes both the conjugate base and the electron localization in the CO_2 moiety. In contrast when the water molecule acts as a sixth ligand, the corresponding transition state geometry changes significantly (see figure S4) and is higher in energy (over 10 kcal/mol).

The second protonation is accompanied by the cleavage of the C−O bond to form the carbonyl intermediate [Fe(qpy)(H_2O)(CO)]$^{2+}$(^{2}[**4Fe**(6)]$^+$) and water. The process is exergonic by −1.4 kcal/mol (coupled to H_2CO_3), but the pK_a is significantly lower (9 units) than the first protonation. The barrier is the highest in the cycle at 17.9 kcal/mol, making this step rate limiting. The transition state involves a weak interaction of the phenol with the metal center resulting in significant distortion in the complex (see figure 14 (c)). The high

oxidation state results in a weak Fe-CO interaction making the CO release and regeneration of the catalyst exergonic and barrierless. The protonation steps are summarized in table 2.

The barrier for the second protonation using the stronger acid H_2CO_3 is 13.2 kcal/mol which is 4.7 kcal/mol lower than the barrier with phenol (see table 2 and see figure S6 (b) for the structure of the TS). Consequently, the stronger acid should significantly increase the catalytic activity. Therefore, a stronger acid could drive the second protonation efficiently *without* a further third reduction (*vide infra*).

Table 2: Possible pathways for the protonation processes in the catalytic cycle for $[Fe^{II}(qpy)(H_2O)_2]^{2+}$. Activation energies ($\Delta G^{\ddagger}$) are reported in kcal/mol and use phenol as a proton source; $\Delta G^{\ddagger}$ reported in parenthesis correspond to activation energies with carbonic acid as a proton source.

Reaction				pK_a	$\Delta G^{\ddagger}$
1 st protonation:	^{3}[**2Fe**(5)]^0 +H^+	$\longrightarrow$	^{5}[**3Fe**(5)]$^+$	25	1.7
2 nd protonation:	^{5}[**3Fe**(5)]$^+$ +H^+ +L	$\longrightarrow$	^{1}[**4Fe**(6)]$^{2+}$ +H_2O	16	17.9 (13.2)
2 nd protonation:	^{4}[**3Fe**(5)]^0 +H^+	$\longrightarrow$	^{2}[**4Fe**(5)]$^{1+}$ +H_2O	24	15.6

The uptake of a third electron is possible for the doubly reduced CO_2, CO_2H or CO intermediates. All discussed pathways for a third reduction are summarized in table 3. The reduction of the CO_2 adduct ^{3}[**2Fe**(5)]^0 (resulting in ^{6}[**2Fe**(5)]$^-$) is unlikely as the computed reduction potential is more negative than −1.8 V. In contrast, the reduction of the carboxy intermediate ^{5}[**3Fe**(5)]$^+$ to ^{4}[**3Fe**(5)]^0 appears at a milder potential with a computed reduction potential of −1.47 V. This is 110 mV less than the potential required for the second reduction. The mild potential is readily rationalized as the qpy π^* orbitals in ^{5}[**3Fe**(5)]$^+$ are not occupied. In addition, both forward and backward reaction barriers are high (rate limiting) and consequently the ^{5}[**3Fe**(5)]$^+$ should accumulate and have a significant lifetime, making a reduction after a single protonation likely. At last, the third reduction can also occur for the carbonyl intermediate ^{1}[**4Fe**(6)]$^{2+}$ to ^{2}[**4Fe**(5)]$^+$ at a mild reduction potential of −0.97 V vs Fc^+/Fc which is in good agreement with the experimentally observed re-oxidation peak at −1.09 V. The additional electron strengthens the backbonding of the

π acidic carbonyl ligand. However, CO release is exergonic and barrierless for the doubly reduced carbonyl intermediate $^2[\mathbf{4Fe}(6)]^+$; consequently, reduction at that stage is unlikely.

Table 3: Possible pathways for the third reduction in the catalytic cycle for $[Fe^{II}(qpy)(H_2O)_2]^{2+}$. Reduction potential are reported in V against the Fc^+/Fc couple. For reference: the computed second reduction of $[Fe^{II}(qpy)(H_2O)_2]^{2+}$ is -1.58 V (from $^4[\mathbf{1Fe}(5)]^+$ to $^1[\mathbf{1Fe}(4)]^0$)

(Half)-Reaction				E^0
CO_2 intermediate:	$^3[\mathbf{2Fe}(5)]^0 + e^-$	$\longrightarrow$	$^6[\mathbf{2Fe}(5)]^-$	-1.85
CO_2H intermediate:	$^5[\mathbf{3Fe}(5)]^+ + e^-$	$\longrightarrow$	$^4[\mathbf{3Fe}(5)]^0$	-1.47
CO intermediate:	$^1[\mathbf{4Fe}(6)]^{2+} + e^-$	$\longrightarrow$	$^2[\mathbf{4Fe}(5)]^+ + L$	-0.97

The subsequent second protonation of the triply reduced $^4[\mathbf{3Fe}(5)]^0$ is both faster (with a barrier of 15.6 kcal/mol) and thermodynamically more favorable (with a pK_a of 24) than the second protonation after only two reductions ($pK_a = 16$, barrier: 17.9 kcal/mol) as the reduction not only destabilizes the reactant, but also stabilizes the product. CO release from $^2[\mathbf{4Fe}(5)]^+$ becomes endergonic (2.0 kcal/mol), but barrierless. Thus, the reduction of the carboxy intermediate $^5[\mathbf{3Fe}(5)]^+$ facilitates the second protonation step both kinetically and thermodynamically (see table 2) albeit at the cost of an endergonic CO release. In addition, a second reduction (fourth overall) of the carbonyl species $^2[\mathbf{4Fe}(5)]^+$ has a calculated potential of -1.45 V vs Fc^+/Fc which is lower than the second reduction of the initial complex, **1Fe**. The accumulation of $^2[\mathbf{4Fe}(5)]^+$ is observed experimentally by a reoxidation peak in the CV experiments and is likely to contribute to the low FE of that catalyst (*vide infra*). The FE was improved experimentally by irradiation with UV-light which induces a low to high spin transition and facilitates the CO release versus a further reduction of the carbonyl intermediate. These findings agree with the CV experiments under CO, where a further reduction of the singly reduced carbonyl intermediate was observed at -1.42 V to yield $^1[\mathbf{4Fe}(5)]^0$. The calculated free energy for CO dissociation from the doubly reduced carbonyl $^1[\mathbf{4Fe}(5)]^0$ is 5.0 kcal/mol which does not justify the experimental observations that

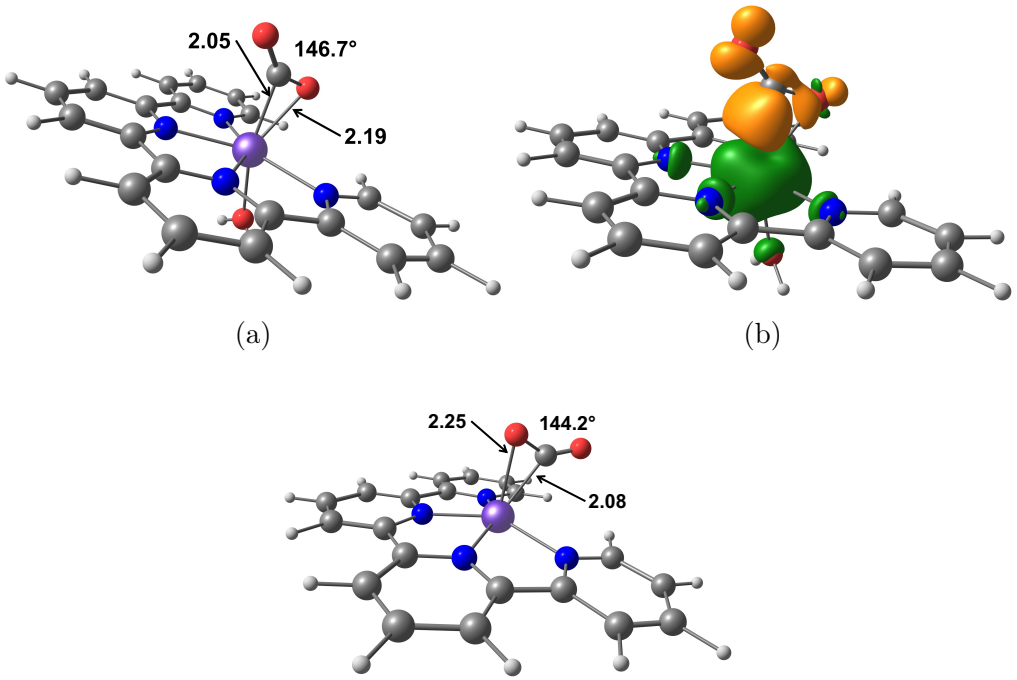

(a) (b)

(c)

Figure 12: Geometrical parameters of both possible CO_2 adduct intermediates of the Iron catalyst (a) after one reduction yielding ^{4}[**2Fe**(6)]$^+$; (b) Spin density of ^{4}[**2Fe**(6)]$^+$ which indicates the formation of a $CO_2^{\cdot -}$, (c) after two reductions yielding ^{3}[**2Fe**(5)]^0.

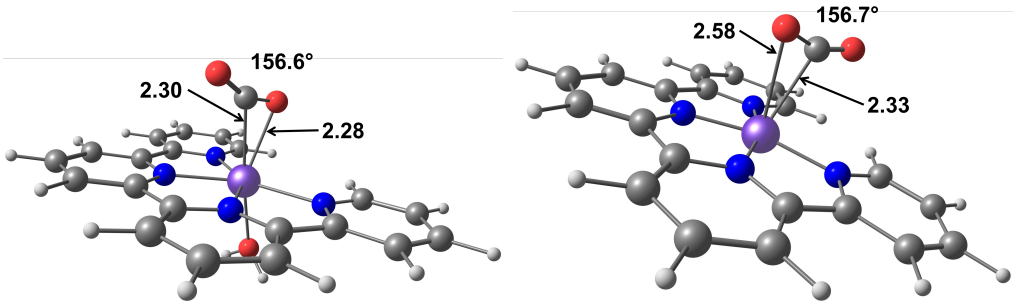

(a) (b)

Figure 13: Geometrical parameters of both transition states yielding the corresponding CO_2 adducts of the iron catalyst after (a) one reduction and (b) two reductions.

^{1}[**4Fe**(5)]^0 poisons the catalyst. However, we find that if the CO release would proceed via a spin transition on the triplet surface, the minimum energy crossing point of the singlet and triplet surfaces along the Fe−C bond is over 20 kcal/mol higher in energy (at a Fe−C bond distance of ∼2.2 Å, see figure S12 (a)). We further note, that ^{1}[**4Fe**(5)]^0 could be the starting point of a more sophisticated degradation pathway. This was observed for the nickel cyclam system, where the formation of a $NiCO_4$ was detected and the addition of CO scavengers increased the activity.[54] Another possibility would be the decomposition of the catalyst yielding metallic iron on the electrode. Further experimental insights are necessary to determine the exact degradation pathway. We investigated possible intermediates and found that upon binding of a second carbonyl, a partial dissociation of the qpy is observed (see figure S12 (b)).

The analysis of a large variety of intermediates showed that two steps in the the catalytic mechanism can proceed via different channels: (i) the binding of CO_2 can occur after one or two reductions (ECE vs EEC mechanism) – our calculations indicate that the ECE mechanism is preferred – (ii) the second protonation can occur after two reductions or after a third reduction where the latter results in a lower barrier and better thermodynamics at the cost of an endergonic CO release. The population of both channels depends on the lifetime of the carboxy intermediate ^{5}[**3Fe**(5)]$^+$, which should be significant due to the large barriers for both protonation steps. Hence, a third reduction at this step seems likely for ^{5}[**3Fe**(5)]$^+$. The rate limiting step is the second protonation. Similar barrier heights were reported by Carter *et al.*[48] for the [Re(bpy)$(CO)_3$Cl] catalyst using a comparable computational set-up and methanol as proton source.

An important aspect of a good CO_2 reduction catalyst is the selectivity for CO2RR over HER. A possible HER mechanism is depicted in the appendix in figure S8. The formation of a hydride from the proposed active species of the catalyst ^{6}[**2Fe**(5)]$^+$ is thermodynamically not favorable as the pK_a for this step is negative. If it is assumed that the CO2RR mechanism proceeds mainly via the ECE channel, then the formation of a hydride should not be possible

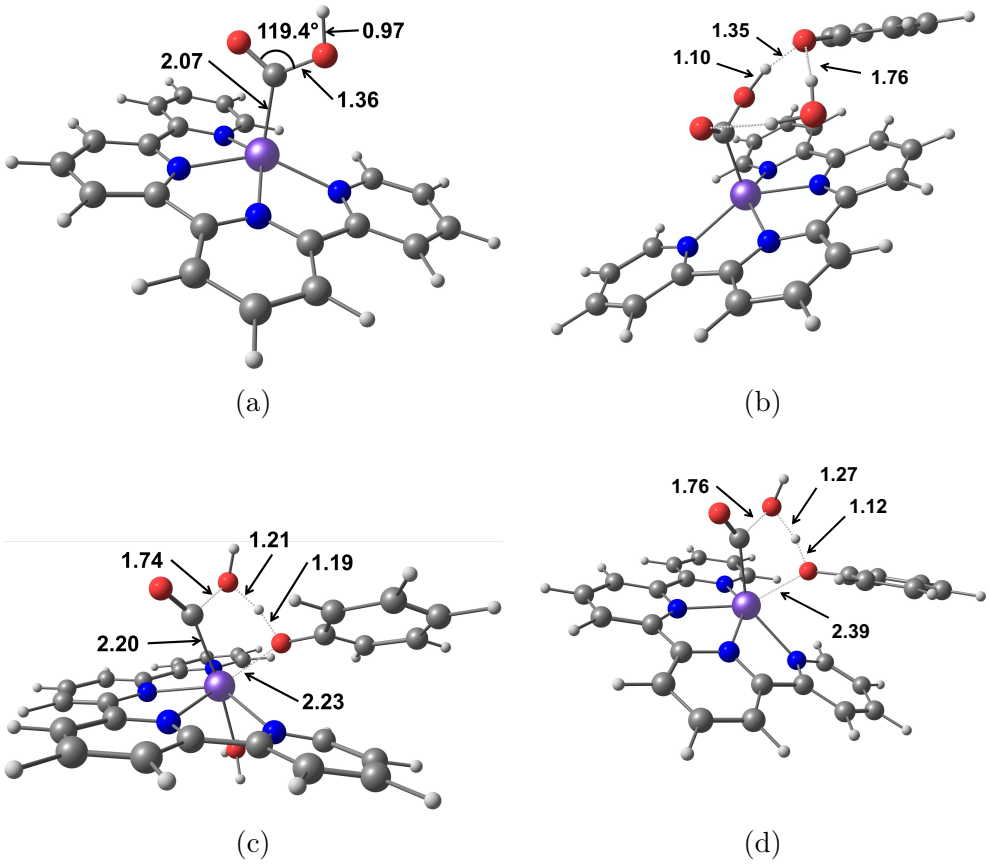

Figure 14: Geometrical parameters of (a) the protonated carboxy intermediate $^{5}[\mathbf{3Fe}(5)]^{2+}$; (b) the transition state for the first protonation step (quintet surface); (c) the transition state for the second protonation step using phenol as the proton source after two reduction steps (quintet surface); (d) the transition state for the second protonation step using phenol as the proton source after a third reduction (quartet surface).

and the catalyst can operate even in very acidic conditions with high selectivity. These findings can be related to the fact that the reductions are mainly ligand based for the Fe catalyst (*vide supra*) which yields a Lewis acidic metal center. Hence, the formation of a hydride is unfavorable. These findings are in line with the experimentally observed high selectivity of over 99% CO in the CPE experiments.[75]

The in-depth analysis of possible catalytic pathways, side reactions, and degradation pathways allows us to rationalize modifications to improve the activity: First, further facilitating the endergonic CO_2 binding after the first reduction will provide not only more driving force for CO_2 addition but also should result in a high selectivity vs HER even in acidic conditions. Thus, a modification of the ligand framework to stabilize the bound CO_2 either via a well-positioned hydrogen bonding donor,[70,71,116] or through electrostatic interactions[69] in the secondary coordination sphere would be beneficial. This concept is well established in bio-inspired catalyst design to enhance catalytic activity.[21,23,117–120] Secondly, to achieve a higher FE, a singly reduced carbonyl intermediate must be avoided. However, our analysis shows that a third reduction at the carboxy intermediate is necessary to improve both kinetics and thermodynamics of the second protonation step. Alternatively, our calculations indicate that a stronger acid (e.g. H_2CO_3) is also capable of driving the second protonation efficiently *without* a third reduction; thus, avoiding the accumulation of a reduced carbonyl intermediate which deactivates a degradation pathway and increases FE.

Comparison and Discussion

After the in-depth analysis of each system, the Co and Fe catalysts can be compared step-wise and an energetic diagram comparing the most likely pathways of both catalyst is depicted in figure 15:

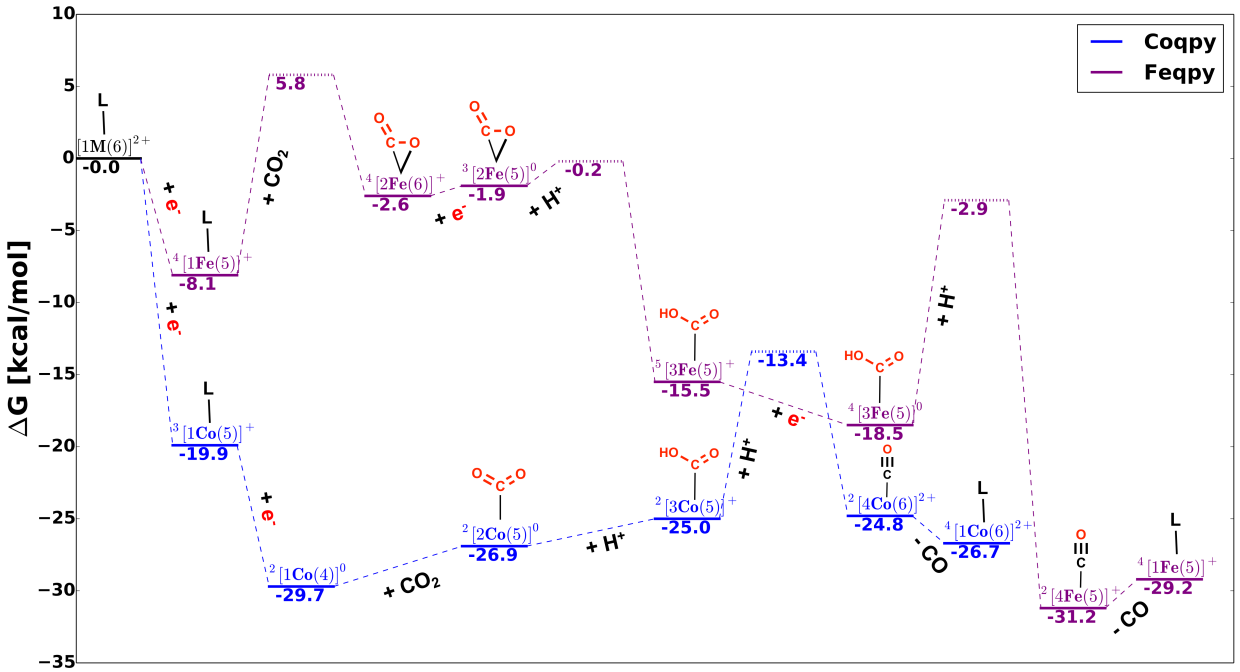

Figure 15: Free energy landscape of the most likely CO2RR pathways of both Coqpy and Feqpy; for the reduction steps, a potential of -1.6 V vs Fc^+/Fc is applied; for the protonation steps, phenol is used to estimate barriers and carbonic acid for free energies (see main text for justification); solid lines correspond to intermediate states and dashed lines to transition states; the energy difference for the total reaction energy in the two cycles stems from using different functionals as the pKa of H_2CO_3 is 12.6 with B3LYP-D3 and 14.7 with ωB97X-D.

Reduction: The $[Co^{II}qpy(H_2O)_2]^{2+}$ catalyst exhibits a ligand-based first reduction and a highly delocalized second reduction. The second excess electron is stabilized by a π type metal ligand bond (with significant metal contribution) between a Co t_{2g} type d orbital and a qpy π^* orbital (see figure 16 (a)). The second reduction is accompanied by a ligand loss which induces a spin transition to a low spin state and notable rearrangement of the ligand framework (twist). These two factors could explain the experimentally observed slow kinetics for this reduction.

The reduction process for the Fe catalyst is markedly different: The $[Fe^{II}qpy(H_2O)_2]^{2+}$ catalyst exhibits two ligand based reductions in the low-lying qpy π^* orbitals (see figure 16 (b)). The iron d orbitals are less suitable for mixing with the qpy π^* orbitals which results in little metal contribution to the singly and doubly reduced states. This leads to significantly more negative reduction potentials but faster kinetics. The doubly reduced intermediates of both cycles $^2[\mathbf{1Co}(4)]^0$ and $^3[\mathbf{1Fe}(4)]^0$ are contrasted in the MO diagram in figure 16.

CO_2 Binding: In the cobalt system, the subsequent CO_2 binding and activation is fast (barrierless) and slightly endergonic. The doubly reduced catalyst $^2[\mathbf{1Co}(4)]^0$ binds CO_2 in an η^1-κC binding mode where a low spin d^8 Co(I) center interacts with CO_2 via a σ type bond from the doubly occupied metal d_{z^2} to the CO_2 LUMO. The binding of CO_2 to a singly reduced complex was not possible suggesting an EEC mechanism for CO_2 binding.

In contrast, the Fe center remains Lewis acidic throughout the reduction process which governs CO_2 binding via an η^2 binding mode. The $CO_2^{\cdot-}$ moiety is stabilized by two pathways: first, by delocalizing some electron density from the CO_2-π^* orbital into the unoccupied (in the β-space) Fe-d_{xz} orbital via a π-type bond; second, by a dative bond from the oxygen lone pair. This allows binding and activation of CO_2 to a *singly* reduced catalyst which is supported by experimental evidence. In both cases the binding and activation process is endergonic with a significant barrier. However, CO_2 binding to a doubly reduced catalyst much slower. This can be explained by the weakened O−Fe (of the CO_2) interaction upon the second reduction which is already significant in the transition state. The computed second reduction of the singly reduced CO_2 adduct is at a similar potential as the second reduction of the catalyst. All this taken into account, CO_2 binding most likely proceeds via reduction-CO_2 binding-reduction (ECE) mechanism. Two factors can explain why the η^2 binding mode is not observed in the Co catalyst: first, the softer Co metal center; second, the additional d electron in Co (in comparison to Fe) yields doubly occupied t_{2g} type orbitals in all spin states, thus preventing a π type interaction of the CO_2 LUMO and the Co. The

key MOs for both the Co and Fe CO_2 adducts are depicted in figure 17.

Protonation: In the Co system, the first protonation is barrierless yielding a doubly reduced COOH moiety bound to an unreduced complex. The second protonation is coupled to the C−O bond cleavage yielding a carbonyl complex and water. This step has a barrier of 11.6 kcal/mol making it rate limiting (and only barrier) in the cycle.

In the Fe system, both protonation reactions have barriers of 1.7 and 17.9 kcal/mol. The second protonation is concerted with the C−O bond cleavage and is the rate limiting step. The barriers are significantly higher for the Fe catalyst, which is in line with the reported difference in activity.

Regeneration: The subsequent CO release to regenerate the catalyst is exergonic and barrierless due to the high oxidation state of the central complex in both cases. The Co catalyst has overall only one low barrier (11.6 kcal/mol) which aligns with the high k_{cat} observed for this catalyst making it one of the fastest molecular CO_2 to CO reduction catalysts. The Fe catalyst on the other hand has two significant barriers, for CO_2 addition (13.9 kcal/mol) and the second protonation (15.6 kcal/mol) rationalizing the lower experimentally observed k_{cat}.

Possible Third Reduction: For the Co catalyst, an alternative three reduction pathway (EEEC) is feasible at a more negative potential. In addition, a third reduction is feasible for each intermediate species at lower potentials than the inital second reduction (see figure S9). This pathway is able to use water efficiently as the proton source but suffers from a very endergonic CO release.

For the Fe catalyst, the barriers for both protonation steps result in an accumulation of the carboxy intermediate which can be further reduced at a mild potential. The third reduction facilitates the second protonation both thermodynamically and kinetically (barrier: 15.6 kcal/mol); however, the subsequent CO release is slightly endergonic which could lead to another reduction of the carbonyl intermediate posing a dead end for catalysis. This could explain the low Faradaic efficiency of the catalyst and the increase of FE due to UV

irradiation.

Possible Improvements: Based on our proposed cycle for the Co system, further tuning of the metal-ligand interaction for the doubly reduced intermediate via electron withdrawing or releasing substituents can alter both the overpotential and catalytic activity: (i) a $-$F group slightly decreases both rate limiting barrier and overpotential; (ii) a $-NH_2$ group markedly increases the reduction potential and also markedly decreases the rate limiting barrier. This opens up the possibility of entering a pathway via the four coordinated doubly reduced species (if a non coordinating acid is used). Thus, could increase k_{cat} *without* an increase of overpotential by proceeding via a different intermediate.

The ECE mechanism proposed for the Fe system makes it extremely robust against a possible HER side reaction. The analysis of a possible HER pathway revealed that the formation of a hydride intermediate from the singly reduced catalyst is only feasible under extremely acidic conditions. This opens up the possibility to operate with stronger acids without a loss in selectivity. Our calculations show that the barriers for the rate limiting second protonation is significantly lower (13.2 kcal/mol); thus, a stronger acid could drive the reaction effectively *without* a third reduction. This would increase both FE and maximum TOF by avoiding the accumulation of an carbonyl intermediate. Furthermore, the modification of the ligand framework to incorporate a moiety in the second coordination sphere could stabilize the bound CO_2 (either via electrostatics or hydrogen bonding) and should facilitate the endergonic CO_2 addition.

Conclusion

In summary, we investigated the catalytic mechanisms of the experimentally reported Fe and Co quaterpyridine molecular electrocatalysts for the two-electron, two-proton reduction of CO_2 to CO using electronic structure calculations (DFT). We report possible catalytic and degradation pathways which are in line with the detailed experimental efforts of Robert *et*

al.[75] Furthermore, we provide an in-depth analysis of the electronic structure of intermediates to understand what factors affect the different pathways of both catalysts.

The $[Co^{II}qpy(H_2O)_2]^{2+}$ catalyst exhibits a ligand-based first reduction and a highly delocalized second reduction. The CO_2 binding proceeds via η^1-κC binding mode, is only possible after two reductions, and is barrierless (EEC mechanism). The subsequent first protonation is barrierless as well. The second protonation is rate limiting (11.6 kcal/mol) followed by a barrierless CO release. The introduction of substituents on the qpy ligand can decrease overpotential or increase the turnover rates. However, a fluorine substituent can slightly improve both and could also increase solubility in aqueous solvents. The amino substituent could also decrease overpotential and turn over rates by proceeding via a different intermediate.

The $[Fe^{II}qpy(H_2O)_2]^{2+}$ catalyst exhibits two ligand based reductions in the low-lying qpy π^* orbitals and binds CO_2 in an η^2 binding mode. This interaction enables CO_2 binding to a singly and doubly reduced catalyst. The binding of CO_2 after a single reduction is kinetically preferred, suggesting an ECE mechanism. Both protonation steps have significantly higher barriers than for the Co catalyst, and the second protonation is rate limiting (17.9 kcal/mol). A third reduction is likely to happen for the carboxy intermediate and reduces the barrier for the second protonation (15.6 kcal/mol) but results in an endergonic CO release. We show that the Fe complex could be a more efficient catalyst with a stronger acid without decreased selectivity towards CO2RR vs HER. This could prevent a third reduction and thus avoid a possible degradation pathway.

Between the two metal systems, the key difference is the more favorable metal d orbital/qpy π^* orbital interaction in the Co system. This becomes apparent when comparing the metal character of the doubly reduced intermediates in figure 16. In the Co catalyst, this leads to greater metal contribution in the first two reductions, resulting in milder reduction potentials and a softer metal center. The subsequent binding and activation of CO_2 relies on a metal base binding to the nucleophilic carbon of the CO_2 in an η^1-κC binding mode.

Binding to a singly reduced Co catalyst was not possible since the metal center is most likely "stuck in the middle" in terms of Lewis acidity. In case of the Fe catalyst, the metal center remains Lewis acidic with mainly ligand based reductions. This leads to a different mechanism of binding and activating CO_2 via an η^2 binding mode which benefits from a Lewis acidic metal center that can bind CO_2 after a single reduction. The key MOs for both the Co and Fe CO_2 adducts are depicted in figure 17.

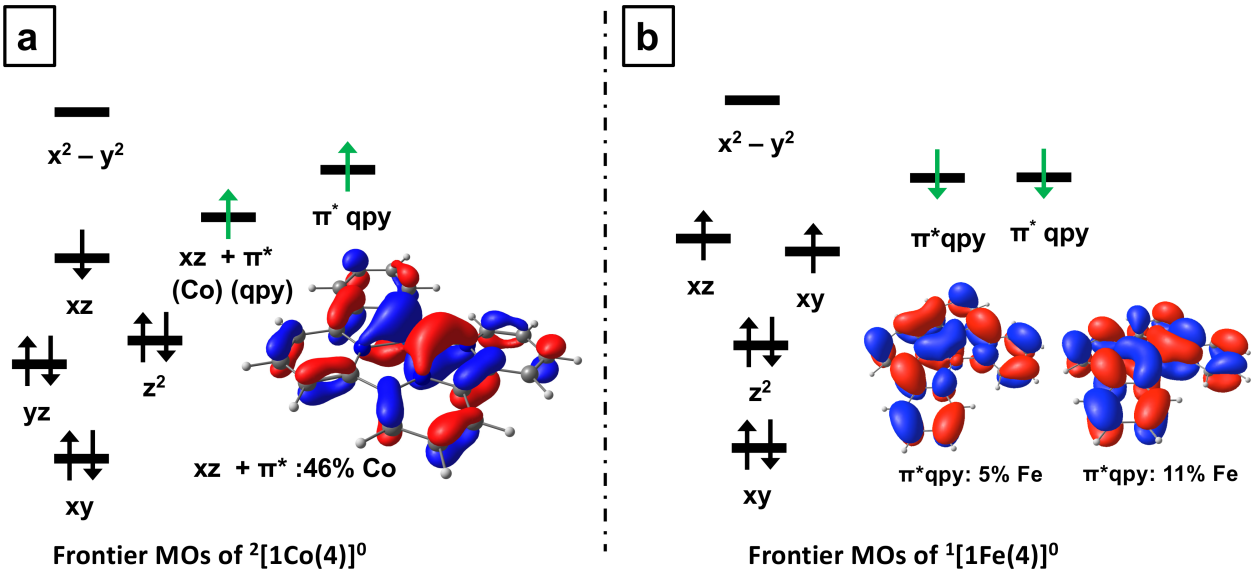

Figure 16: Schematic MO diagram of both doubly reduced intermediates a) $^2[\mathbf{1Co}(4)]^0$ and b) $^1[\mathbf{1Fe}(4)]^0$. The green arrows indicate the extra electrons due to both reductions. The MO shown in panel (a) illustrates the delocalized π type metal (d_{xz}) ligand (π^*) bond to stabilize the excess electron; the MOs in panel (b) illustrate the mainly ligand based character of the two reductions.

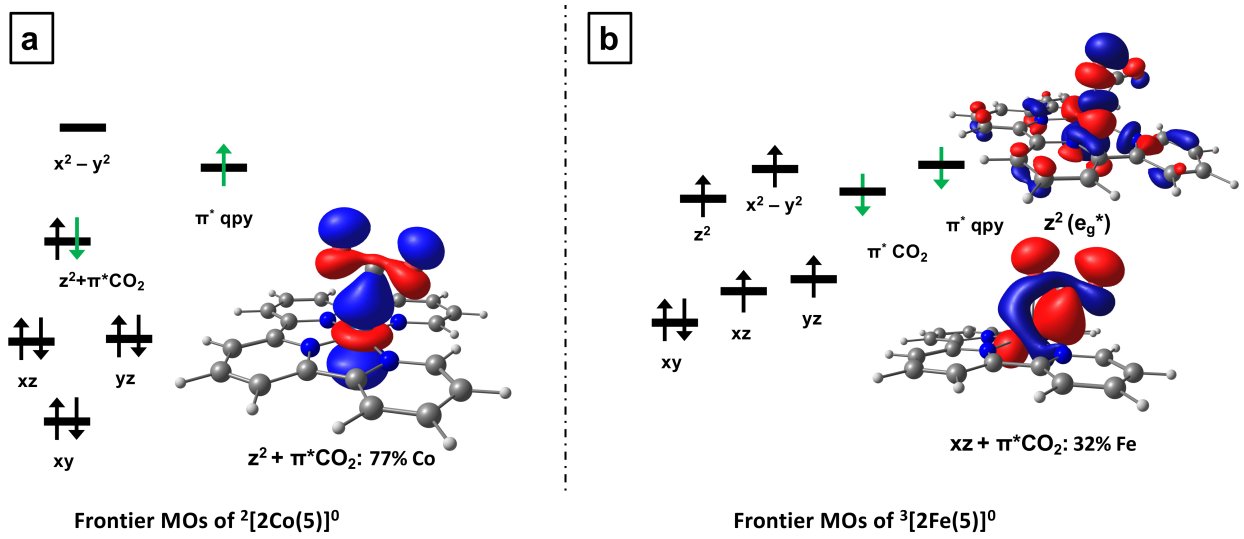

Figure 17: Schematic MO diagram of both doubly reduced CO_2 adducts a) ^{2}[**1Co**(4)]^0 and b) ^{3}[**1Fe**(4)]^0. The green arrows indicate the extra electrons due to both reductions. The MO in panel (a) illustrates the σ type interaction of the Co-d_{z^2} orbital and the CO_2 LUMO leading to the η^1 binding mode in the Co system; the MOs in panel (b) illustrate the two ways the CO_2 is stabilized in an η^2 binding mode in the Fe system: (i) by a π type CO_2 LUMO Fe-d_{xz} bond; (ii) by a dative O−Fe bond from the oxygen lone pair.

Acknowledgement

This work was supported by the U.S. Department of Energy, Office of Science, Office of Advanced Scientific Computing, and Office of Basic Energy Sciences, via the Scientific Discovery through Advanced Computing (SciDAC) program. We thank Dip Hait, Joonho Lee, Chris Stein, Jeff Derrick, Chris Chang and Marc Robert for fruitful discussions. DBKC acknowledges UC LEADS undergraduate fellowship and DCAG acknowledges UCB undergraduate fellowship.

Supporting Information Available

Additional structural information of important intermediates; HER cycles and larger cycles including a third reduction; probe of functional sensitivity using B3LYP, ωB97X-D, ωB97M-V, PBE0 and TPSSh; CASSCF calculations of both doubly reduced intermediates; all XYZ coordinates and sample inputs.

References

(1) Lewis, N. S.; Nocera, D. G. Powering the planet: Chemical challenges in solar energy utilization. *Proc. Natl. Acad. Sci. U.S.A.* **2006**, *103*, 15729–15735.

(2) Gust, D.; Moore, T. A.; Moore, A. L. Solar fuels via artificial photosynthesis. *Acc. Chem. Res.* **2009**, *42*, 1890–1898.

(3) De Luna, P.; Hahn, C.; Higgins, D.; Jaffer, S. A.; Jaramillo, T. F.; Sargent, E. H. What would it take for renewably powered electrosynthesis to displace petrochemical processes? *Science* **2019**, *364*, eaav3506.

(4) de Klerk, A.; Furimsky, E. Catalysis in the refining of Fischer–Tropsch syncrude. *Platinum Metals Rev* **2011**, *55*, 263–267.

(5) Verma, S.; Kim, B.; Jhong, H.-R. M.; Ma, S.; Kenis, P. J. A. A Gross-Margin Model for Defining Technoeconomic Benchmarks in the Electroreduction of CO2. *ChemSusChem* **2016**, *9*, 1972–1979.

(6) Appel, A. M.; Bercaw, J. E.; Bocarsly, A. B.; Dobbek, H.; DuBois, D. L.; Dupuis, M.; Ferry, J. G.; Fujita, E.; Hille, R.; Kenis, P. J. A.; Kerfeld, C. A.; Morris, R. H.; Peden, C. H. F.; Portis, A. R.; Ragsdale, S. W.; Rauchfuss, T. B.; Reek, J. N. H.; Seefeldt, L. C.; Thauer, R. K.; Waldrop, G. L. Frontiers, Opportunities, and Challenges in Biochemical and Chemical Catalysis of CO2 Fixation. *Chem. Rev.* **2013**, *113*, 6621–6658.

(7) Kumar, B.; Llorente, M.; Froehlich, J.; Dang, T.; Sathrum, A.; Kubiak, C. P. Photochemical and photoelectrochemical reduction of CO2. *Annu. Rev. Phys. Chem* **2012**, *63*, 541–569.

(8) Savéant, J.-M. Molecular catalysis of electrochemical reactions. Mechanistic aspects. *Chem. Rev.* **2008**, *108*, 2348–2378.

(9) Takeda, H.; Cometto, C.; Ishitani, O.; Robert, M. Electrons, Photons, Protons and Earth-Abundant Metal Complexes for Molecular Catalysis of CO2 Reduction. *ACS Catal.* **2017**, *7*, 70–88.

(10) Francke, R.; Schille, B.; Roemelt, M. Homogeneously catalyzed electroreduction of carbon dioxide—methods, mechanisms, and catalysts. *Chem. Rev.* **2018**, *118*, 4631–4701.

(11) Dalle, K. E.; Warnan, J.; Leung, J. J.; Reuillard, B.; Karmel, I. S.; Reisner, E. Electro- and solar-driven fuel synthesis with first row transition metal complexes. *Chem. Rev.* **2019**, *119*, 2752–2875.

(12) Zhang, B.; Sun, L. Artificial photosynthesis: opportunities and challenges of molecular catalysts. *Chem. Soc. Rev.* **2019**, *48*, 2216–2264.

(13) Kuhl, K. P.; Cave, E. R.; Abram, D. N.; Jaramillo, T. F. New insights into the electrochemical reduction of carbon dioxide on metallic copper surfaces. *Energy Environ. Sci* **2012**, *5*, 7050–7059.

(14) Zhao, G.; Huang, X.; Wang, X.; Wang, X. Progress in catalyst exploration for heterogeneous CO2 reduction and utilization: a critical review. *J. Mater. Chem. A* **2017**, *5*, 21625–21649.

(15) Razzak, S. A.; Ali, S. A. M.; Hossain, M. M.; deLasa, H. Biological CO2 fixation with production of microalgae in wastewater–a review. *Renew. Sustain. Energy Rev* **2017**, *76*, 379–390.

(16) García de Arquer, F. P.; Dinh, C.-T.; Ozden, A.; Wicks, J.; McCallum, C.; Kirmani, A. R.; Nam, D.-H.; Gabardo, C.; Seifitokaldani, A.; Wang, X.; Li, Y. C.; Li, F.; Edwards, J.; Richter, L. J.; Thorpe, S. J.; Sinton, D.; Sargent, E. H. CO2 electrolysis to multicarbon products at activities greater than 1 A cm^{-1}. *Science* **2020**, *367*, 661–666.

(17) Lee, C. H.; Kanan, M. W. Controlling H+ vs CO2 Reduction Selectivity on Pb Electrodes. *ACS Catal.* **2015**, *5*, 465–469.

(18) Hori, Y.; Kikuchi, K.; Murata, A.; Suzuki, S. Production of methane and ethylene in electrochemical reduction of carbon dioxide at copper electrode in aqueous hydrogencarbonate solution. *Chem. Lett.* **1986**, *15*, 897–898.

(19) Goodpaster, J. D.; Bell, A. T.; Head-Gordon, M. Identification of Possible Pathways for C-C Bond Formation during Electrochemical Reduction of CO2: New Theoretical Insights from an Improved Electrochemical Model. *J. Phys. Chem. Lett* **2016**, *7*, 1471–1477.

(20) Garza, A. J.; Bell, A. T.; Head-Gordon, M. Mechanism of CO2 reduction at copper surfaces: Pathways to C2 products. *ACS Catal.* **2018**, *8*, 1490–1499.

(21) Roy, S.; Sharma, B.; Pécaut, J.; Simon, P.; Fontecave, M.; Tran, P. D.; Derat, E.; Artero, V. Molecular Cobalt Complexes with Pendant Amines for Selective Electrocatalytic Reduction of Carbon Dioxide to Formic Acid. *J. Am. Chem. Soc.* **2017**, *139*, 3685–3696.

(22) Savéant, J.-M. Proton Relays in Molecular Catalysis of Electrochemical Reactions: Origin and Limitations of the Boosting Effect. *Angew. Chem. Int. Ed.* **2019**, *58*, 2125–2128.

(23) Nichols, A. W.; Machan, C. W. Secondary-Sphere Effects in Molecular Electrocatalytic CO2 Reduction. *FRONT CHEM* **2019**, *7*.

(24) Ren, S.; Joulié, D.; Salvatore, D.; Torbensen, K.; Wang, M.; Robert, M.; Berlinguette, C. P. Molecular electrocatalysts can mediate fast, selective CO2 reduction in a flow cell. *Science* **2019**, *365*, 367–369.

(25) Lin, S.; Diercks, C. S.; Zhang, Y.-B.; Kornienko, N.; Nichols, E. M.; Zhao, Y.; Paris, A. R.; Kim, D.; Yang, P.; Yaghi, O. M.; Chang, C. J. Covalent organic frameworks comprising cobalt porphyrins for catalytic CO2 reduction in water. *Science* **2015**, *349*, 1208–1213.

(26) Kornienko, N.; Zhao, Y.; Kley, C. S.; Zhu, C.; Kim, D.; Lin, S.; Chang, C. J.; Yaghi, O. M.; Yang, P. Metal-Organic Frameworks for Electrocatalytic Reduction of Carbon Dioxide. *J. Am. Chem. Soc.* **2015**, *137*, 14129–14135.

(27) Hod, I.; Sampson, M. D.; Deria, P.; Kubiak, C. P.; Farha, O. K.; Hupp, J. T. Fe-Porphyrin-Based Metal-Organic Framework Films as High-Surface Concentration, Heterogeneous Catalysts for Electrochemical Reduction of CO2. *ACS Catal.* **2015**, *5*, 6302–6309.

(28) Wang, H.; Zeng, Z.; Xu, P.; Li, L.; Zeng, G.; Xiao, R.; Tang, Z.; Huang, D.; Tang, L.; Lai, C.; Jiang, D.; Liu, Y.; Yi, H.; Qin, L.; Ye, S.; Ren, X.; Tang, W. Recent progress in covalent organic framework thin films: fabrications, applications and perspectives. *Chem. Soc. Rev.* **2019**, *48*, 488–516.

(29) Oh, S.; Gallagher, J. R.; Miller, J. T.; Surendranath, Y. Graphite-Conjugated Rhenium Catalysts for Carbon Dioxide Reduction. *J. Am. Chem. Soc.* **2016**, *138*, 1820–1823.

(30) Wang, M.; Chen, L.; Lau, T.-C.; Robert, M. A hybrid Co quaterpyridine complex/carbon nanotube catalytic material for CO2 reduction in water. *Angew. Chem. Int. Ed.* **2018**, *57*, 7769–7773.

(31) Kaminsky, C. J.; Wright, J.; Surendranath, Y. Graphite-conjugation enhances porphyrin electrocatalysis. *ACS Catal.* **2019**, *9*, 3667–3671.

(32) Zhu, M.; Chen, J.; Huang, L.; Ye, R.; Xu, J.; Han, Y.-F. Covalently grafting cobalt

porphyrin onto carbon nanotubes for efficient CO2 electroreduction. *Angew. Chem. Int. Ed.* **2019**, *58*, 6595–6599.

(33) Zhanaidarova, A.; Jones, S. C.; Despagnet-Ayoub, E.; Pimentel, B. R.; Kubiak, C. P. Re (tBu-bpy)(CO) 3Cl Supported on Multi-Walled Carbon Nanotubes Selectively Reduces CO2 in Water. *J. Am. Chem. Soc.* **2019**, *141*, 17270–17277.

(34) Smith, P. T.; Nichols, E. M.; Cao, Z.; Chang, C. J. Hybrid Catalysts for Artificial Photosynthesis: Merging Approaches from Molecular, Materials, and Biological Catalysis. *Acc. Chem. Res.* **2020**, *53*, 575–587.

(35) Costentin, C.; Passard, G.; Robert, M.; Savéant, J.-M. Pendant acid–base groups in molecular catalysts: H-bond promoters or proton relays? Mechanisms of the conversion of CO2 to CO by electrogenerated iron (0) porphyrins bearing prepositioned phenol functionalities. *J. Am. Chem. Soc.* **2014**, *136*, 11821–11829.

(36) Costentin, C.; Savéant, J.-M. Concepts and tools for mechanism and selectivity analysis in synthetic organic electrochemistry. *Proc. Natl. Acad. Sci. U.S.A.* **2019**, *116*, 11147–11152.

(37) Derrick, J. S.; Loipersberger, M.; Chatterjee, R.; Iovan, D. A.; Smith, P. T.; Chakarawet, K.; Yano, J.; Long, J. R.; Head-Gordon, M.; Chang, C. J. Metal–Ligand Cooperativity via Exchange Coupling Promotes Iron-Catalyzed Electrochemical CO2 Reduction at Low Overpotentials. *J. Am. Chem. Soc.* **2020**,

(38) Benson, E. E.; Sampson, M. D.; Grice, K. A.; Smieja, J. M.; Froehlich, J. D.; Friebel, D.; Keith, J. A.; Carter, E. A.; Nilsson, A.; Kubiak, C. P. The Electronic States of Rhenium Bipyridyl Electrocatalysts for CO2 Reduction as Revealed by X-ray Absorption Spectroscopy and Computational Quantum Chemistry. *Angew. Chem., Int. Ed.* **2013**, *52*, 4841–4844.

(39) Römelt, C.; Song, J.; Tarrago, M.; Rees, J. A.; van Gastel, M.; Weyhermüller, T.; DeBeer, S.; Bill, E.; Neese, F.; Ye, S. Electronic Structure of a Formal Iron(0) Porphyrin Complex Relevant to CO2 Reduction. *Inorg. Chem.* **2017**, *56*, 4745–4750.

(40) Machan, C. W. Recent advances in spectroelectrochemistry related to molecular catalytic processes. *Curr Opin Electrochem* **2019**, *15*, 42 – 49.

(41) Sampson, M. D.; Froehlich, J. D.; Smieja, J. M.; Benson, E. E.; Sharp, I. D.; Kubiak, C. P. Direct observation of the reduction of carbon dioxide by rhenium bipyridine catalysts. *Energy. Environ. Sci.* **2013**, *6*, 3748–3755.

(42) Lee, K. J.; Elgrishi, N.; Kandemir, B.; Dempsey, J. L. Electrochemical and spectroscopic methods for evaluating molecular electrocatalysts. *Nat. Rev. Chem.* **2017**, *1*, 0039.

(43) Hohenberg, P.; Kohn, W. Inhomogeneous electron gas. *Phys. Rev.* **1964**, *136*, B864.

(44) Kohn, W.; Sham, L. J. Self-consistent equations including exchange and correlation effects. *Phys. Rev.* **1965**, *140*, A1133.

(45) Mardirossian, N.; Head-Gordon, M. Thirty years of density functional theory in computational chemistry: an overview and extensive assessment of 200 density functionals. *Mol. Phys.* **2017**, *115*, 2315–2372.

(46) Chan, B.; Gill, P. M.; Kimura, M. Assessment of DFT Methods for Transition Metals with the TMC151 Compilation of Data Sets and Comparison with Accuracies for Main-Group Chemistry. *J. Chem. Theory Comput* **2019**, *15*, 3610–3622.

(47) Song, J.; Klein, E. L.; Neese, F.; Ye, S. The Mechanism of Homogeneous CO2 Reduction by Ni(cyclam): Product Selectivity, Concerted Proton-Electron Transfer and C-O Bond Cleavage. *Inorg. Chem.* **2014**, *53*, 7500–7507.

(48) Keith, J. A.; Grice, K. A.; Kubiak, C. P.; Carter, E. A. Elucidation of the selectivity of proton-dependent electrocatalytic CO2 reduction by fac-Re (bpy)(CO) 3Cl. *J. Am. Chem. Soc.* **2013**, *135*, 15823–15829.

(49) Riplinger, C.; Sampson, M. D.; Ritzmann, A. M.; Kubiak, C. P.; Carter, E. A. Mechanistic contrasts between manganese and rhenium bipyridine electrocatalysts for the reduction of carbon dioxide. *J. Am. Chem. Soc.* **2014**, *136*, 16285–16298.

(50) Riplinger, C.; Carter, E. A. Influence of weak Brønsted acids on electrocatalytic CO2 reduction by manganese and rhenium bipyridine catalysts. *ACS Catal.* **2015**, *5*, 900–908.

(51) Fisher, B. J.; Eisenberg, R. Electrocatalytic reduction of carbon dioxide by using macrocycles of nickel and cobalt. *J. Am. Chem. Soc.* **1980**, *102*, 7361–7363.

(52) Beley, M.; Collin, J.-P.; Ruppert, R.; Sauvage, J.-P. Nickel (II)-cyclam: an extremely selective electrocatalyst for reduction of CO 2 in water. *ChemComm* **1984**, 1315–1316.

(53) Beley, M.; Collin, J. P.; Ruppert, R.; Sauvage, J. P. Electrocatalytic reduction of carbon dioxide by nickel cyclam2+ in water: study of the factors affecting the efficiency and the selectivity of the process. *J. Am. Chem. Soc.* **1986**, *108*, 7461–7467.

(54) Froehlich, J. D.; Kubiak, C. P. The homogeneous reduction of CO2 by [Ni (cyclam)]+: increased catalytic rates with the addition of a CO scavenger. *J. Am. Chem. Soc.* **2015**, *137*, 3565–3573.

(55) Hawecker, J.; Lehn, J.-M.; Ziessel, R. Electrocatalytic reduction of carbon dioxide mediated by Re (bipy)(CO) 3 Cl (bipy= 2, 2'-bipyridine). *ChemComm* **1984**, 328–330.

(56) Smieja, J. M.; Kubiak, C. P. Re(bipy-tBu)(CO)3Cl–improved Catalytic Activity for

Reduction of Carbon Dioxide: IR-Spectroelectrochemical and Mechanistic Studies. *Inorg. Chem.* **2010**, *49*, 9283–9289.

(57) Smieja, J. M.; Sampson, M. D.; Grice, K. A.; Benson, E. E.; Froehlich, J. D.; Kubiak, C. P. Manganese as a Substitute for Rhenium in CO2 Reduction Catalysts: The Importance of Acids. *Inorg. Chem.* **2013**, *52*, 2484–2491.

(58) Sampson, M. D.; Nguyen, A. D.; Grice, K. A.; Moore, C. E.; Rheingold, A. L.; Kubiak, C. P. Manganese Catalysts with Bulky Bipyridine Ligands for the Electrocatalytic Reduction of Carbon Dioxide: Eliminating Dimerization and Altering Catalysis. *J. Am. Chem. Soc.* **2014**, *136*, 5460–5471.

(59) Machan, C. W.; Sampson, M. D.; Chabolla, S. A.; Dang, T.; Kubiak, C. P. Developing a Mechanistic Understanding of Molecular Electrocatalysts for CO2 Reduction using Infrared Spectroelectrochemistry. *Organometallics* **2014**, *33*, 4550–4559.

(60) Machan, C. W.; Stanton, C. J.; Vandezande, J. E.; Majetich, G. F.; Schaefer, H. F.; Kubiak, C. P.; Agarwal, J. Electrocatalytic Reduction of Carbon Dioxide by Mn(CN)(2,2'-bipyridine)(CO)3: CN Coordination Alters Mechanism. *Inorg. Chem.* **2015**, *54*, 8849–8856.

(61) Chabolla, S. A.; Machan, C. W.; Yin, J.; Dellamary, E.; Sahu, S.; Gianneschi, N.; Gilson, M.; Tezcan, F.; Kubiak, C. Bio-inspired CO2 reduction by a rhenium tricarbonyl bipyridine-based catalyst appended to amino acids and peptidic platforms: incorporating proton relays and hydrogen-bonding functional groups. *Faraday Discuss.* **2017**, *198*, 279–300.

(62) Sung, S.; Li, X.; Wolf, L. M.; Meeder, J. R.; Bhuvanesh, N. S.; Grice, K. A.; Panetier, J. A.; Nippe, M. Synergistic effects of imidazolium-functionalization on fac-Mn (CO) 3 bipyridine catalyst platforms for electrocatalytic carbon dioxide reduction. *J. Am. Chem. Soc.* **2019**, *141*, 6569–6582.

(63) Matson, B. D.; McLoughlin, E. A.; Armstrong, K. C.; Waymouth, R. M.; Sarangi, R. Effect of Redox Active Ligands on the Electrochemical Properties of Manganese Tricarbonyl Complexes. *Inorg. Chem.* **2019**, *58*, 7453–7465.

(64) Myren, T. H.; Alherz, A.; Thurston, J. R.; Stinson, T. A.; Huntzinger, C. G.; Musgrave, C. B.; Luca, O. R. Mn-Based Molecular Catalysts for the Electrocatalytic Disproportionation of CO_2 into CO and CO_3^-. *ACS Catal.* **2020**, *10*, 1961–1968.

(65) Hammouche, M.; Lexa, D.; Savéant, J.; Momenteau, M. Catalysis of the electrochemical reduction of carbon dioxide by iron ("0") porphyrins. *J. Electroanal. Chem.* **1988**, *249*, 347–351.

(66) Costentin, C.; Drouet, S.; Robert, M.; Savéant, J.-M. A Local Proton Source Enhances CO2 Electroreduction to CO by a Molecular Fe Catalyst. *Science* **2012**, *338*, 90–94.

(67) Costentin, C.; Robert, M.; Savéant, J.-M.; Tatin, A. Efficient and selective molecular catalyst for the CO2-to-CO electrochemical conversion in water. *Proc. Natl. Acad. Sci.* **2015**, *112*, 6882–6886.

(68) Costentin, C.; Passard, G.; Robert, M.; Savéant, J.-M. Ultraefficient homogeneous catalyst for the CO2-to-CO electrochemical conversion. *Proc. Natl. Acad. Sci.* **2014**, *111*, 14990–14994.

(69) Azcarate, I.; Costentin, C.; Robert, M.; Savéant, J.-M. Through-space charge interaction substituent effects in molecular catalysis leading to the design of the most efficient catalyst of CO_2-to-CO electrochemical conversion. *J. Am. Chem. Soc.* **2016**, *138*, 16639–16644.

(70) Zee, D. Z.; Nippe, M.; King, A. E.; Chang, C. J.; Long, J. R. Tuning Second Coordination Sphere Interactions in Polypyridyl–Iron Complexes to Achieve Selective Electrocatalytic Reduction of Carbon Dioxide to Carbon Monoxide. *Inorg. Chem.* **2020**, *59*, 5206–5217.

(71) Loipersberger, M.; Zee, D. Z.; Panetier, J. A.; Chang, C. J.; Long, J. R.; Head-Gordon, M. Computational Study of an Iron(II) Polypyridine Electrocatalyst for CO2 Reduction: Key Roles for Intramolecular Interactions in CO2 Binding and Proton Transfer. *Inorg. Chem.* **2020**, *59*, 8146–8160.

(72) Su, X.; McCardle, K. M.; Chen, L.; Panetier, J. A.; Jurss, J. W. Robust and Selective Cobalt Catalysts Bearing Redox-Active Bipyridyl-N-heterocyclic Carbene Frameworks for Electrochemical CO2 Reduction in Aqueous Solutions. *ACS Catal.* **2019**, *9*, 7398–7408.

(73) Che, C.-M.; Chan, C.-W.; Yang, S.-M.; Guo, C.-X.; Lee, C.-Y.; Peng, S.-M. Synthesis, properties and crystal structures of iron-(II) and-(III) complexes of 2, 2': 6', 2 ": 6 ", 2"'-quaterpyridine. *J. Chem. Soc., Dalton Trans.* **1995**, 2961–2966.

(74) Lam, K.-M.; Wong, K.-Y.; Yang, S.-M.; Che, C.-M. Cobalt and nickel complexes of 2, 2': 6', 2": 6", 2"'-quaterpyridine as catalysts for electrochemical reduction of carbon dioxide. *J. Chem. Soc., Dalton Trans.* **1995**, 1103–1107.

(75) Cometto, C.; Chen, L.; Lo, P.-K.; Guo, Z.; Lau, K.-C.; Anxolabéhère-Mallart, E.; Fave, C.; Lau, T.-C.; Robert, M. Highly selective molecular catalysts for the CO2-to-CO electrochemical conversion at very low overpotential. Contrasting Fe vs Co quaterpyridine complexes upon mechanistic studies. *ACS Catal.* **2018**, *8*, 3411–3417.

(76) Cometto, C.; Chen, L.; Anxolabéhère-Mallart, E.; Fave, C.; Lau, T.-C.; Robert, M. Molecular electrochemical catalysis of the CO2-to-CO conversion with a Co complex: A cyclic voltammetry mechanistic investigation. *Organometallics* **2018**, *38*, 1280–1285.

(77) Guo, Z.; Chen, G.; Cometto, C.; Ma, B.; Zhao, H.; Groizard, T.; Chen, L.; Fan, H.; Man, W.-L.; Yiu, S.-M.; Lau, K.-C.; Lau, T.-C.; Robert, M. Selectivity control of CO

versus HCOO- production in the visible-light-driven catalytic reduction of CO 2 with two cooperative metal sites. *Nat. Catal.* **2019**, *2*, 801–808.

(78) Guo, Z.; Cheng, S.; Cometto, C.; Anxolabéhère-Mallart, E.; Ng, S.-M.; Ko, C.-C.; Liu, G.; Chen, L.; Robert, M.; Lau, T.-C. Highly efficient and selective photocatalytic CO2 reduction by iron and cobalt quaterpyridine complexes. *J. Am. Chem. Soc.* **2016**, *138*, 9413–9416.

(79) Cometto, C.; Chen, L.; Mendoza, D.; Lassalle-Kaiser, B.; Lau, T.-C.; Robert, M. An Iron Quaterpyridine Complex as Precursor for the Electrocatalytic Reduction of CO2 to Methane. *ChemSusChem* **2019**, *12*, 4500–4505.

(80) Pati, P. B.; Wang, R.; Boutin, E.; Diring, S.; Jobic, S.; Barreau, N.; Odobel, F.; Robert, M. Photocathode functionalized with a molecular cobalt catalyst for selective carbon dioxide reduction in water. *Nat. Commun* **2020**, *11*, 1–9.

(81) Pavlishchuk, V. V.; Addison, A. W. Conversion constants for redox potentials measured versus different reference electrodes in acetonitrile solutions at 25°C. *Inorg. Chim. Acta* **2000**, *298*, 97 – 102.

(82) Sampson, M. D.; Kubiak, C. P. Manganese electrocatalysts with bulky bipyridine ligands: Utilizing Lewis acids to promote carbon dioxide reduction at low overpotentials. *J. Am. Chem. Soc.* **2016**, *138*, 1386–1393.

(83) Bonin, J.; Maurin, A.; Robert, M. Molecular catalysis of the electrochemical and photochemical reduction of CO2 with Fe and Co metal based complexes. Recent advances. *Coord. Chem. Rev.* **2017**, *334*, 184–198.

(84) Azcarate, I.; Costentin, C.; Robert, M.; Savéant, J.-M. Dissection of electronic substituent effects in multielectron–multistep molecular catalysis. Electrochemical CO2-to-CO conversion catalyzed by iron porphyrins. *J. Phys. Chem. C* **2016**, *120*, 28951–28960.

(85) Fukuzumi, S.; Lee, Y.-M.; Ahn, H. S.; Nam, W. Mechanisms of catalytic reduction of CO 2 with heme and nonheme metal complexes. *Chemical science* **2018**, *9*, 6017–6034.

(86) Davethu, P. A.; de Visser, S. P. CO2 Reduction on an Iron-Porphyrin Center: A Computational Study. *The Journal of Physical Chemistry A* **2019**, *123*, 6527–6535.

(87) Shao, Y.; Gan, Z.; Epifanovsky, E.; Gilbert, A. T. B.; Wormit, M.; Kussmann, J.; Lange, A. W.; Behn, A.; Deng, J.; Feng, X.; Ghosh, D.; Goldey, M.; Horn, P. R.; Jacobson, L. D.; Kaliman, I.; Khaliullin, R. Z.; Kús, T.; Landau, A.; Liu, J.; Proynov, E. I.; Rhee, Y. M.; Richard, R. M.; Rohrdanz, M. A.; Steele, R. P.; Sundstrom, E. J.; Woodcock III, H. L.; Zimmerman, P. M.; Zuev, D.; Albrecht, B.; Alguire, E.; Austin, B.; Beran, G. J. O.; Bernard, Y. A.; Berquist, E.; Brandhorst, K.; Bravaya, K. B.; Brown, S. T.; Casanova, D.; Chang, C.-M.; Chen, Y.; Chien, S. H.; Closser, K. D.; Crittenden, D. L.; Diedenhofen, M.; DiStasio Jr., R. A.; Dop, H.; Dutoi, A. D.; Edgar, R. G.; Fatehi, S.; Fusti-Molnar, L.; Ghysels, A.; Golubeva-Zadorozhnaya, A.; Gomes, J.; Hanson-Heine, M. W. D.; Harbach, P. H. P.; Hauser, A. W.; Hohenstein, E. G.; Holden, Z. C.; Jagau, T.-C.; Ji, H.; Kaduk, B.; Khistyaev, K.; Kim, J.; Kim, J.; King, R. A.; Klunzinger, P.; Kosenkov, D.; Kowalczyk, T.; Krauter, C. M.; Lao, K. U.; Laurent, A.; Lawler, K. V.; Levchenko, S. V.; Lin, C. Y.; Liu, F.; Livshits, E.; Lochan, R. C.; Luenser, A.; Manohar, P.; Manzer, S. F.; Mao, S.-P.; Mardirossian, N.; Marenich, A. V.; Maurer, S. A.; Mayhall, N. J.; Oana, C. M.; Olivares-Amaya, R.; O'Neill, D. P.; Parkhill, J. A.; Perrine, T. M.; Peverati, R.; Pieniazek, P. A.; Prociuk, A.; Rehn, D. R.; Rosta, E.; Russ, N. J.; Sergueev, N.; Sharada, S. M.; Sharmaa, S.; Small, D. W.; Sodt, A.; Stein, T.; Stück, D.; Su, Y.-C.; Thom, A. J. W.; Tsuchimochi, T.; Vogt, L.; Vydrov, O.; Wang, T.; Watson, M. A.; Wenzel, J.; White, A.; Williams, C. F.; Vanovschi, V.; Yeganeh, S.; Yost, S. R.; You, Z.-Q.; Zhang, I. Y.; Zhang, X.; Zhou, Y.; Brooks, B. R.; Chan, G. K. L.; Chipman, D. M.; Cramer, C. J.; Goddard III, W. A.; Gordon, M. S.; Hehre, W. J.;

Klamt, A.; Schaefer III, H. F.; Schmidt, M. W.; Sherrill, C. D.; Truhlar, D. G.; Warshel, A.; Xua, X.; Aspuru-Guzik, A.; Baer, R.; Bell, A. T.; Besley, N. A.; Chai, J.-D.; Dreuw, A.; Dunietz, B. D.; Furlani, T. R.; Gwaltney, S. R.; Hsu, C.-P.; Jung, Y.; Kong, J.; Lambrecht, D. S.; Liang, W.; Ochsenfeld, C.; Rassolov, V. A.; Slipchenko, L. V.; Subotnik, J. E.; Van Voorhis, T.; Herbert, J. M.; Krylov, A. I.; Gill, P. M. W.; Head-Gordon, M. Advances in molecular quantum chemistry contained in the Q-Chem 4 program package. *Mol. Phys.* **2015**, *113*, 184–215.

(88) Chai, J.-D.; Head-Gordon, M. Long-range corrected hybrid density functionals with damped atom-atom dispersion corrections. *Phys. Chem. Chem. Phys.* **2008**, *10*, 6615–6620.

(89) Becke, A. D. Density-functional exchange-energy approximation with correct asymptotic behavior. *Phys. Rev. A* **1988**, *38*, 3098.

(90) Lee, C.; Yang, W.; Parr, R. G. Development of the Colle-Salvetti correlation-energy formula into a functional of the electron density. *Phys. Rev. B* **1988**, *37*, 785.

(91) Becke, A. D. Density-functional thermochemistry. III. The role of exact exchange. *J. Chem. Phys.* **1993**, *98*, 5648–5652.

(92) Grimme, S.; Ehrlich, S.; Goerigk, L. Effect of the damping function in dispersion corrected density functional theory. *J. Comput. Chem* **2011**, *32*, 1456–1465.

(93) Weigend, F.; Ahlrichs, R. Balanced basis sets of split valence, triple zeta valence and quadruple zeta valence quality for H to Rn: Design and assessment of accuracy. *Phys. Chem. Chem. Phys* **2005**, *7*, 3297–3305.

(94) A new method for incorporating solvent effect into the classical, ab initio molecular orbital and density functional theory frameworks for arbitrary shape cavity. *Chem. Phys. Lett.* **1995**, *240*, 253 – 260.

(95) Garza, A. J.; Pakhira, S.; Bell, A. T.; Mendoza-Cortes, J. L.; Head-Gordon, M. Reaction mechanism of the selective reduction of CO_2 to CO by a tetraaza $[Co^{II}\ N_4\ H]^{2+}$ complex in the presence of protons. *Phys. Chem. Chem. Phys.* **2018**, *20*, 24058–24064.

(96) Garza, A. J.; Bell, A. T.; Head-Gordon, M. Is subsurface oxygen necessary for the electrochemical reduction of CO2 on copper? *J. Phys. Chem. Lett.* **2018**, *9*, 601–606.

(97) Alongi, K. S.; Shields, G. C. In *Chapter 8 - Theoretical Calculations of Acid Dissociation Constants: A Review Article*; Wheeler, R. A., Ed.; Annu Rep Comput Chem; Elsevier, 2010; Vol. 6; pp 113 – 138.

(98) Kelly, C. P.; Cramer, C. J.; Truhlar, D. G. Single-Ion Solvation Free Energies and the Normal Hydrogen Electrode Potential in Methanol, Acetonitrile, and Dimethyl Sulfoxide. *J. Phys. Chem. B* **2007**, *111*, 408–422.

(99) Bhattacharjee, A.; Andreiadis, E. S.; Chavarot-Kerlidou, M.; Fontecave, M.; Field, M. J.; Artero, V. A Computational Study of the Mechanism of Hydrogen Evolution by Cobalt(Diimine-Dioxime) Catalysts. *Chem.: Eur. J* **2013**, *19*, 15166–15174.

(100) Raamat, E.; Kaupmees, K.; Ovsjannikov, G.; Trummal, A.; Kütt, A.; Saame, J.; Koppel, I.; Kaljurand, I.; Lipping, L.; Rodima, T. Acidities of strong neutral Brønsted acids in different media. *Journal of Physical Organic Chemistry* **2013**, *26*, 162–170.

(101) Aktaş, A. H.; Şanlı, N.; Pekcan, G. Spectrometric Determination of pK. *Acta Chim. Slov* **2006**, *53*, 214–218.

(102) Matsubara, Y. Unified Benchmarking of Electrocatalysts in Noninnocent Second Coordination Spheres for CO2 Reduction. *ACS Energy Lett.* **2019**, *4*, 1999–2004.

(103) Kelly, C. P.; Cramer, C. J.; Truhlar, D. G. Adding explicit solvent molecules to continuum solvent calculations for the calculation of aqueous acid dissociation constants. *J. Phys. Chem. A* **2006**, *110*, 2493–2499.

(104) Fu, Y.; Liu, L.; Yu, H.-Z.; Wang, Y.-M.; Guo, Q.-X. Quantum-Chemical Predictions of Absolute Standard Redox Potentials of Diverse Organic Molecules and Free Radicals in Acetonitrile. *J. Am. Chem. Soc.* **2005**, *127*, 7227–7234.

(105) Konezny, S. J.; Doherty, M. D.; Luca, O. R.; Crabtree, R. H.; Soloveichik, G. L.; Batista, V. S. Reduction of Systematic Uncertainty in DFT Redox Potentials of Transition-Metal Complexes. *J. Phys. Chem. C* **2012**, *116*, 6349–6356.

(106) Jensen, K. P.; Roos, B. O.; Ryde, U. Performance of density functionals for first row transition metal systems. *J. Chem. Phys.* **2007**, *126*, 014103.

(107) Moltved, K. A.; Kepp, K. P. Chemical bond energies of 3d transition metals studied by density functional theory. *J. Chem. Theory Comput* **2018**, *14*, 3479–3492.

(108) Moltved, K. A.; Kepp, K. P. The Metal Hydride Problem of Computational Chemistry: Origins and Consequences. *J. Phys. Chem. A* **2019**, *123*, 2888–2900.

(109) Jensen, K. P.; Cirera, J. Accurate computed enthalpies of spin crossover in iron and cobalt complexes. *J. Phys. Chem. A* **2009**, *113*, 10033–10039.

(110) Cirera, J.; Via-Nadal, M.; Ruiz, E. Benchmarking density functional methods for calculation of state energies of first row spin-crossover molecules. *Inorg. Chem.* **2018**, *57*, 14097–14105.

(111) Arumugam, K.; Becker, U. Computational redox potential predictions: applications to inorganic and organic aqueous complexes, and complexes adsorbed to mineral surfaces. *Minerals* **2014**, *4*, 345–387.

(112) Hait, D.; Head-Gordon, M. Delocalization errors in density functional theory are essentially quadratic in fractional occupation number. *J. Phys. Chem. Lett.* **2018**, *9*, 6280–6288.

(113) Thom, A. J.; Sundstrom, E. J.; Head-Gordon, M. LOBA: a localized orbital bonding analysis to calculate oxidation states, with application to a model water oxidation catalyst. *Phys. Chem. Chem. Phys.* **2009**, *11*, 11297–11304.

(114) Bhugun, I.; Lexa, D.; Savéant, J.-M. Catalysis of the electrochemical reduction of carbon dioxide by iron (0) porphyrins: Synergystic effect of weak Brönsted acids. *J. Am. Chem. Soc.* **1996**, *118*, 1769–1776.

(115) Aresta, M.; Nobile, C. F.; Albano, V. G.; Forni, E.; Manassero, M. New nickel–carbon dioxide complex: synthesis, properties, and crystallographic characterization of (carbon dioxide)-bis (tricyclohexylphosphine) nickel. *ChemComm* **1975**, 636–637.

(116) Nichols, E. M.; Derrick, J. S.; Nistanaki, S. K.; Smith, P. T.; Chang, C. J. Positional effects of second-sphere amide pendants on electrochemical CO2 reduction catalyzed by iron porphyrins. *Chem. Sci.* **2018**, *9*, 2952–2960.

(117) Haviv, E.; Azaiza-Dabbah, D.; Carmieli, R.; Avram, L.; Martin, J. M.; Neumann, R. A thiourea tether in the second coordination sphere as a binding site for CO2 and a proton donor promotes the electrochemical reduction of CO2 to CO catalyzed by a rhenium bipyridine-type complex. *J. Am. Chem. Soc.* **2018**, *140*, 12451–12456.

(118) Hong, D.; Tsukakoshi, Y.; Kotani, H.; Ishizuka, T.; Kojima, T. Visible-Light-Driven Photocatalytic CO2 Reduction by a Ni(II) Complex Bearing a Bioinspired Tetradentate Ligand for Selective CO Production. *J. Am. Chem. Soc.* **2017**, *139*, 6538–6541.

(119) Dubey, A.; Nencini, L.; Fayzullin, R. R.; Nervi, C.; Khusnutdinova, J. R. Bio-Inspired Mn(I) Complexes for the Hydrogenation of CO2 to Formate and Formamide. *ACS Catal.* **2017**, *7*, 3864–3868.

(120) Ngo, K. T.; McKinnon, M.; Mahanti, B.; Narayanan, R.; Grills, D. C.; Ertem, M. Z.; Rochford, J. Turning on the Protonation-First Pathway for Electrocatalytic CO2 Re-

duction by Manganese Bipyridyl Tricarbonyl Complexes. *J. Am. Chem. Soc.* **2017**, *139*, 2604–2618.

Graphical TOC Entry